Ultra-depleted melt refertilization of mantle peridotites in a large intra-transform domain (Doldrums Fracture Zone; 7-8ºN, Mid Atlantic Ridge)

Camilla Sani[1], Alessio Sanfilippo[1,2*], Carlotta Ferrando[1,3], Alexander A. Peyve[4], Sergey G. Skolotonev[4], Filippo Muccini[5], Alberto Zanetti[2], Valentin Basch[1], Camilla Palmiotto[6], Enrico Bonatti[6,7] and Marco Ligi[6]

[1] Dipartimento di Scienze della Terra e dell'Ambiente, Università di Pavia, Via Ferrata 1a, 27100, Pavia, Italy.

[2] Istituto Geoscienze e Georisorse – CNR, Pavia, Via Ferrata 1a, 27100, Pavia, Italy

[3] Centre de Recherches Pétrographiques et Géochimiques, Université de Lorraine, CNRS, Vandœuvre-lès-Nancy, France.

[4] Geological Institute of the Russian Academy of Science, Moscow, Russia

[5] Istituto Nazionale Geofisica e Vulcanologia, Via di Vigna Murata 605, 00143 Roma, Italy

[6] Istituto di Scienze Marine – CNR, Via Gobetti 101, 40129 Bologna, Italy

[7] Lamont Doherty Earth Observatory, Columbia University, 61 Route 9W, Palisades, New York 10964, USA

*Corresponding author email: alessio.sanfilippo@unipv.it

ABSTRACT

The Doldrums transform system offsets the Equatorial Mid Atlantic Ridge by ~630 km at 7-8º N. This transform system consists of four intra-transform spreading centers (ITRs) bounded by five transform faults. The northernmost ITR is linked to the MAR axis by a ~180 km-long transform. Here, during two *R/V A. N. Strakhov* expeditions (S06 and S09), mantle peridotites were dredged along the transverse and median ridge of the transform, across the western flank of the ITR valley. Residual harzburgites were mainly sampled along the northern Doldrums transform valley, whereas plagioclase-bearing peridotites showing evidence for melt-rock interaction characterize the ITR domain. Petrological and geochemical observations reinforced by geochemical modelling are used to define the behaviour of trace elements during melt extraction and melt-rock reaction in our rocks. Results suggest that residual peridotites derive from mantle rocks that have undergone a degree of partial melting up to 12%, with melting likely starting at the transition of garnet-spinel stability fields, whereas peridotites which suffered melt-rock reactions have been divided into two types: (i) pl-impregnated peridotites, formed by migration of melts at high porosity and high melt-rock ratio; and (ii) refertilized peridotites, generated at reduced porosity, when small fractions of the same percolating melt crystallized clinopyroxene and minor plagioclase. We suggest that the refertilizing agent was a melt highly depleted in incompatible trace elements, in turn produced by an ultra-depleted mantle source. This mantle experienced previous degrees of melt extraction at the ridge axis, before being transposed laterally along the transform where it melted a second time during the opening of the intra-transform spreading segment.

1. Introduction

The Equatorial portion of the Mid Atlantic Ridge is displaced for several thousands of kilometers towards the east by a series of large offset oceanic transforms. In contrast with the classical idea of oceanic transforms (Wilson, 1965), slow-slip long-offset transform domains are characterized by a wide and lens-shaped zone of deformation bounded by two major fault systems probably active at alternate periods (Ligi et al., 2002). These large oceanic transform domains - also called "megatransforms"- show a broad (>100 km) and complex multi-faults shear zone similarly to the large continental strike-slip systems. The complexity of the plate boundaries at these locations affects fundamentally their thermal structure that in turn controls mantle melting, melt migration, aggregation and emplacement of the lower crust (Bonatti et al., 2003; Ligi et al., 2005; Brunelli et al., 2018). Several authors (e.g., Ligi et al. 2002; 2005; Sclater et al., 2005; Maia et al., 2016) proposed that an extreme thickness of the lithosphere determines the unusual width and complex geometry of megatransforms. Such a strong change in thermal conditions may result in a dramatic reduction of the melting region, together with a deepening of the ductile/brittle transition from 8 to 35 km, as a transform is approached (Ligi et al. 2005;). These peculiar features make lithospheric mantle sections exposed along these large transforms a natural laboratory to test models of mantle melting and melt migration in cold thermal regimes (see also Brunelli et al., 2018).

Observations on MORBs and abyssal peridotites suggest that melt extraction occurs mainly through high-porosity channels (e.g., Kelemen et al., 1995). However, at cold thermal conditions, melt may migrate through grain boundaries, reacting and crystallizing within the solid matrix (Dick and Bullen, 1984). The latter process is enhanced by decreasing temperature and it is generally associated to the crystallization of interstitial mineral assemblages often containing plagioclase as major phase (e.g., Seyler and Bonatti, 1997; Tartarotti et al., 2002; Piccardo et al., 2007; Dick et al., 2010; Warren and Shimizu, 2010), in what is generally called "plagioclase impregnation". Microtextures and geochemical data on

bulk rock and mineral phases, however, indicate that not only plagioclase but also olivine

(e.g., Kelemen et al., 1990; Niu et al., 2004; 2007; Piccardo et al., 2007; Rampone et al.,

2008) clinopyroxene and spinel (e.g., Seyler et al., 2001; 2004; Brunelli et al., 2006; Suhr et

al., 2008; Brunelli and Seyler, 2010; Warren and Shimizu, 2010) crystallize during melt-rock

reactions, depending mainly on pressure, temperature, and, to some extent, on melt

composition and melt mass. The study of melt-percolated peridotites thereby offers a chance

to retrieve fundamental information on the chemical composition of the melt before it is

emplaced in the oceanic crust.

At the Doldrums Fracture Zone (hereafter Doldrums FZ) (7-8 ºN, MAR), the exposure of

portions of mantle sections along fracture zones provides direct access to peridotites that

record melt percolation processes. This complex multi-transform system is characterized by

several short intra-transform spreading segments and transform faults. We describe here a

unique suite of mantle peridotites exposed at the northern intra-transform domain of the

Doldrums FZ (ITR-1, ~8ºN). We show that these peridotites are characterized by a bimodal

composition, ranging from residual after moderate to high degrees of partial melting to

strongly re-fertilized by interaction with migrating melts. Based on geochemical models we

infer an ultra-depleted origin for the melt infiltrating these peridotites that, given their

preferential occurrence within the intra-transform domain, was probably produced by partial

melting of depleted mantle portions, moving away from the MAR axis and re-melted during

the opening of the ITR domain.

2- Structure of the Doldrums megatransform

Among the megatransforms of the Equatorial Atlantic, the Doldrums FZ is arguably the

least studied, although it is a major discontinuity in the Equatorial MAR displacing the axis

from 39.5º to 34º W and extending from 7ºN to 8º N. This 600 km-long and up to 100-km

wide lens-shaped system is observed in the bathymetry (Fig. 1) and includes four intra-

98   transform spreading ridges bounded by five transforms, named from north to south:

99   Doldrums, Vernadsky, northern 7.4° N, southern 7.4° N and Bogdanov (Skolotnev et al.,

100   2020). The offset length of each transform tends to increase towards the north, with a

101   maximum value of ~180 km in the northernmost transform (Doldrums) that, considering an

102   average half-spreading rate of 15 mm/a, corresponds roughly to an age offset of 13 Ma

103   (Skolotnev et al., 2020). Preliminary multibeam survey and dredging were carried out during

104   two expeditions of *R/V Akademik Nikolai Strakhov* (S06 and S09) (Pushcharovsky et al.,

105   1991, 1992). A total of 40 dredges were deployed along the MAR sector north of the

106   Doldrums system, along the transform valley and the axis of the intra-transform spreading

107   ridge connecting Doldrums and Vernadsky transforms (Pushcharovsky et al., 1992) (Fig. 1b).

108   Basement rocks were collected in 23 dredges, of which 15 contained serpentinized mantle

109   peridotites (Fig. 1b and Supplementary Table 1). They are mostly located along the transform

110   valley, in agreement with evidence of exposure of upper mantle rocks in the large transform

111   systems of the Atlantic, such as the 15.20ºN (Pushcharovsky et al., 1988, Kelemen et al.,

112   2004; Suhr et al., 2008), Vema (Bonatti et al., 2003; Brunelli et al., 2006) and Romanche

113   transforms (Bonatti et al., 1996; 2001). We note, however, that peridotites were collected also

114   from the central sector of the active intra-transform ridge segment (ITR-1) at the eastern end

115   of the Doldrums transform, probably due to detachment faulting (Skolotnev et al., 2006;

116   2020).

117   Based on their location in the megatransform system, the peridotites are hereafter

118   subdivided into three groups, indicated with different colours in Fig. 1: (1) North Doldrums

119   transform fault (DTF-N) including dredges deployed along the transverse ridge flanking to

120   the north of the transform valley. Dredge hauls consist mostly of peridotites, with minor

121   basalt rubbles and rare gabbros; (2) South Doldrums transform fault (DTF-S) including

122   dredges from the median ridge, the south wall and the transverse ridge (located ~260 km east

123   of the MAR axis) of the Doldrums transform valley. Samples are mostly peridotites, rare

124 gabbros and pillow basalts; and (3) Intra-transform ridge (ITR-1) including dredges deployed

125 on the rift shoulder and on a dome-shaped structure along the ITR-1 (see Skolotnev et al.,

126 2020 for details on these structures). Here, peridotites are minor, and are commonly

127 associated with deformed gabbros, dolerites and rare basalt rubbles. Deformed rocks and

128 cataclastic textures indicate that the basement was probably exhumed by detachment faulting.

129 In this group, we have also included peridotites collected at the base of Peyve Seamount, a

130 ~20 km-long and ~2000 m-high tectonic structure forming the northern wall of the

131 Vernadsky transform valley. This structure is oriented parallel to the transform and is mostly

132 formed by evolved Ti-Fe oxide-bearing gabbros often showing evidence of high temperature

133 deformation.

134

135 **3-Sample selection and analytical methods**

136 Samples were selected from each Doldrums FZ dredge haul. Major element compositions

137 were acquired on 28 samples, following a preliminary petrographic description. A subset of

138 only 9 samples was suitable for the determination of trace element compositions, the rest

139 being extensively altered. Extensive serpentinization often obliterates the original fabric of

140 the mantle minerals. Where possible, the modal composition of the mineral phases was

141 nonetheless obtained by point counting. Almost 1000 points per section were counted on

142 standard-size thin sections. Serpentine with mesh texture and associated to magnetite was

143 attributed to olivine (ol), whereas bastitic serpentine was attributed to orthopyroxenes (opx).

144 Selected peridotites are harzburgites to cpx-poor lherzolite.

145 Major element compositions were measured by electron probe analysis on a CAMEBAX-

146 Microbeam microanalyzer in the Institute of Geochemistry RAS at an accelerating voltage of

147 15 kV and a current of 30 nA. Major element compositions of ol, opx, cpx, and spinels (sp)

148 are provided in Supplementary Tables 2-5.

149   The trace element composition of clinopyroxenes was analysed on thin sections by laser

150   ablation ICP-MS using a QQQ-ICP-MS Agilent Series 8900 interfaced to a GeoLas 193 nm

151   excimer ablation system (Lambda Physik, Germany) at the CNR–IGG S.S. of Pavia. The

152   ablation system was operated at a 10 Hz repetition rate, 50 μm spot size, with a fluence of

153   about 9 J/cm^2. Helium was used as carrier gas and mixed with Ar downstream of the ablation

154   cell. NIST SRM 610 synthetic glass was used as external standard, whereas ^{44}Ca was adopted

155   as internal standard. Precision and accuracy were assessed from repeated analyses of BRC-2g

156   reference material and resulted better than ±10%. Average element abundances in synthetic

157   glasses NIST SRM 610 were taken from Pearce et al. (1997). Background and signal were

158   measured for about 60 s; signal of standards and unknowns were carefully checked, and the

159   raw data were reduced using the software package GLITTER® (van Achterbergh et al.,

160   2001).

161

162   **4-Textures and major element compositions of the mineral phases**

163   Samples from the DTF-N have commonly a porphyroclastic texture characterized by the

164   alignment of pyroxene porphyroclasts and spinels. Opx are coarse-grained and commonly

165   deformed, showing kink bands and undulose extinction. Large porphyroclasts are locally

166   surrounded by smaller-grained pyroxene neoblasts with well-equilibrated textures and triple

167   grain junctions (Fig. 2a). Cpx occur mostly as deformed porphyroclasts, and rare cpx are

168   found as neoblasts (Fig. 2b). When preserved, olivines show subgrain boundaries and

169   undulose extinction, and large ol crystals are locally replaced by finer neoblasts. Sp occur in

170   the ol matrix as irregular or vermicular grains with lobate texture.

171   Peridotites from the ITR and the DTF-S are mostly granular, but rarely also

172   porphyroclastic. Opx locally exceed 20 mm in size and are mildly deformed. Cpx are mostly

173   found as porphyroclasts. Among these samples, a significant quantity (~20%) contains up to

174   5% pl as microveins crosscutting the original mantle minerals or patches associated with fine-

175   grained opx (Fig. 2c,d). Other samples have very low amount of pl, associated not with opx,

176   but with interstitial cpx, locally forming undeformed films between the deformed

177   porphyroclasts (Fig. 2e). In these samples, cpx are also associated with irregular sp showing

178   lobate shape (Fig. 2f). Similar assemblages have been documented in melt-reacted abyssal

179   peridotites and interpreted as entrapment of small aliquots of unextracted melt in the

180   asthenosphere (Seyler et al., 2004; 2007; Brunelli and Seyler, 2010) or at the lithosphere-

181   asthenosphere boundary (e.g., Suhr et al., 2008). The samples with pl-opx patches will be

182   hereafter named "pl-impregnated", following the idea that large amount of pl-opx patches

183   indicates extensive crystallization of silica-saturated melts within the peridotite matrix (Dick

184   and Bullen, 1984; Tartarotti et al., 2002; Piccardo et al., 2007). On the other hand, samples

185   with interstitial cpx-pl microveins will be hereafter called "refertilized" to indicate relatively

186   low extent of refertilization at low melt mass.

187   The major element mineral compositions of the Doldrums FZ peridotites is highly variable

188   and cover a broad spectrum of abyssal peridotites worldwide. Overall, they have refractory

189   compositions. This geochemical variability is shown in Fig. 3, where we plot the sp Cr# =

190   [Cr/(Cr+Al) mol%] as main proxy for mantle depletion versus Mg# = [Mg/(Mg+Fe) mol%]

191   and TiO_2 in the same phase, and versus variations in Forsterite (Fo) and TiO_2 in coexisting ol

192   and cpx, respectively.

193   Samples from DTF-N have spinels with Cr# and Mg# ranging from 30-50 mol% and 50-

194   70 mol%, respectively (Fig. 3a), and TiO_2 never exceeding 0.1 to 0.2 wt% (Fig. 3b). TiO_2 in

195   cpx is also characteristically low (0.1 wt%; Fig 3d), decreasing at increasing Cr# in

196   coexisting spinels. Consistently, the pyroxenes have high Mg# (cpx = 89-92 mol%; opx = 90-

197   92 mol%) and high Cr_2O_3 (cpx = 1.13-1.61 wt%; opx = 0.96-1.22 wt%). Cr# in pyroxenes

198   displays positive correlations, also plotting within the depleted field of residual abyssal

199   peridotites (Fig. 4b). From mineral compositions, the DTF-N peridotites define a trend typical

200   of fractional melting starting from DM-like compositions (Workman and Hart, 2005).

201   Olivines in these samples are always serpentinized or highly weathered.

202   Different geochemical features are shown by most peridotites collected in the ITR and

203   DTF-S (see Fig. 3). Although the sp Cr# in these samples is similar to that in DTF-N (25-60

204   mol%; Fig. 3a), they are clearly distinct in TiO_2, which commonly exceeds 0.2 wt%, locally

205   up to 1.0 wt% (Fig. 3b). The TiO_2 in spinel is considered a good proxy for interaction with

206   migrating melts (Dick and Bullen, 1984), confirming textural evidence of impregnation in

207   these samples. In agreement with a re-fertilized composition, cpx in ITR and DTF-S

208   peridotites have higher TiO_2 (0.19-0.50 wt%) for a given Cr# in coexisting sp compared to

209   cpx in residual peridotites from DTF-N (Fig. 3d). Similar to the residual peridotites, Cr# of

210   opx and cpx in DTF-S and ITR peridotites show a positive correlation (Fig. 4b). Few ol

211   grains in these rocks are locally preserved from serpentinization. They generally have high Fo

212   (91-89 mol%) and NiO (0.30-0.37 wt%), although the most reacted samples have ol with Fo

213   as low as 88 mol% (Fig. 3c).

214   Cpx from most samples show positive TiO_2 and Na_2O correlations (Fig. 4a). In agreement

215   with textural observation, cpx in ITR and DTF-S peridotites show a bimodal distribution in

216   TiO_2 vs Na_2O space (later sustained by the trace element compositions) (Fig. 4a); pl-

217   peridotites tend to have high TiO_2 and Na_2O concentrations, whereas refertilized peridotites

218   have relatively high Na_2O (0.6-0.5 wt%) but TiO_2 contents comparable to those of the

219   residual peridotites (< 0.2 wt%).

220

221   **5- Clinopyroxene trace element compositions**

222   Nine samples were selected for the analysis of trace elements in cpx. Although the

223   extensive serpentinization limited sample selection, selected samples are representative of the

224   main rock-types in the area. We selected four residual harzburgites from the DTF-N; two pl-

225   impregnated and two refertilized peridotites from the ITR. In addition, we selected one pl-

226   free harzburgite from the base of Peyve Seamount, east of the ITR, in order to characterize

227   the ITR mantle composition before melt-rock reactions. Depending on texture, two to four

228   cpx were selected in each sample; two analyses were carried out per each cpx. Given the very

229   limited intra-sample variability, the analyses were averaged per sample and are provided in

230   Supplementary Table 6 along with their standard deviation. One refertilized sample from the

231   DTF-S (S09-69/2) contains two geochemically distinct typologies of Cpx that, distinguished

232   in porphyroclastic and interstitial varieties, were averaged separately.

233   Cpx in residual peridotites from DTF-N have subparallel chondrite-normalized

234   incompatible element patterns (CI from Anders and Grevesse, 1989) (Fig.5a). They show low

235   M- and H-REE contents (Yb_N = 3.3-5.8), limited M-/H-REE fractionations (($Gd/Yb)_N$ = 0.43-

236   0.61), and very steep L-REE to M-REE patterns (($Ce/Sm)_N$ = 0.07-0.13) but variable

237   enrichments in La (($La/Ce)_N$ = 2.80-5.97) with inversion of the slope (Fig. 5b). Notably, Sr is

238   generally enriched compared to the neighbouring elements (Sr/Sr^* = 0.96-3.23), whereas Zr

239   and Ti show clear negative anomalies (Fig. 5a). These residual cpx show very low Zr/Hf

240   ratios. The same refractory composition is shown by the pl-free harzburgite from the ITR

241   with high fractionated L-REE (($Ce/Sm)_N$ = 0.02) contents and relatively high Yb_N (~5.33).

242   This sample has sp with Cr# =~55 mol% and low TiO_2 (0.15 wt%), and lacks any textural

243   evidence for refertilization, in agreement with its residual character.

244   In agreement with the texture and major element compositions, the CI-normalized patterns

245   of cpx in DTF-S and ITR-1 are distinct for the two typologies of peridotites. Cpx in pl-

246   impregnated peridotites has nearly flat H- to M-REE (($Gd/Yb)_N$ = 0.94-1.13), high Yb (Yb_N =

247   7.38-14.63), and high L-REE to M-REE fractionations (($Ce/Sm)_N$ = 0.04-0.10) (Fig. 5c). In

248   agreement with the presence of pl, they show strong depletion in Eu and Sr compared to

249   neighbouring elements (Eu/Eu^* = 0.59-0.72 and Sr/Sr^* = 0.08-0.22, respectively) and less

250   pronounced Zr and Ti negative anomalies. Cpx in refertilized peridotites (Fig. 5d) have nearly

251   flat patterns, negative M- to H-REE fractionations (($Gd/Yb)_N$ = 0.67-0.52), relatively low M-

252   and H-REE contents (Yb_N = 4-5.05). One sample (S09-69/2) includes cpx occurring both as

253   porphyroclasts and interstitial grains. Although undistinguishable on the basis of M- and H-

254   REE contents, they are characterized by distinct L-REE fractionations that separate the

255   porphyroclasts slightly depleted in L-REE ($(Ce/Sm)_N$ = ~0.3) from interstitial grains with

256   nearly flat REE patterns ($(Ce/Sm)_N$ = ~0.6).

257

258   **6. Discussion**

259   *6.1 Residual character of the Doldrums FZ-North peridotites*

260   The textural and geochemical characteristics of the peridotites from the DTF-N suggest a

261   residual origin. They lack textural evidence of refertilization, and are characterized by

262   depleted compositions plotting on trends expected for fractional melting, namely high Cr#

263   and low TiO_2 in sp (Fig. 3a,b), low incompatible trace elements in cpx and L-REE depletion

264   (see also Johnson et al., 1990) (Fig. 5b). Using the calibration of Hellebrand et al. (2001) we

265   derived degrees of mantle partial melting (*F*) from sp Cr#, obtaining *F* ranging between 13%

266   to 17.5% (Fig. 3a) assuming a pure fractional melting process. Note that these estimates

267   furnish even higher values when critical porosity is included (see Fig. 3 in Hellebrand et al.,

268   2001). These values are inconsistent with the average degree of melting inferred from the

269   basalts physically associated to the DFZ-N residual peridotites (Fig. 1c; Skolotnev et al.,

270   1991) that show Na_8 values ranging from 2.7 to 3.4, corresponding to an average degree of

271   melting from 7 to 12% of a DM source (calculated from the parameterization of Klein and

272   Langmuir, 1987). We note, however, that the use of sp Cr# as melting indicator relies on two

273   main assumptions:

274   *1)* the first is that peridotites are residual from a common protolith having DM-like

275   composition. Based on $^{176}Hf/^{177}Hf$ and $^{143}Nd/^{144}Nd$ co-variations of oceanic peridotites, it is

276   now generally accepted that the upper mantle is constituted by a heterogeneous association of

277   variably depleted domains, locally retaining refractory compositions having depletion ages as

278   old as 1 Ga (Liu et al., 2008; Stracke et al., 2011; 2019; Salters et al., 2011; Mallick et al.,

279   2014; 2015; Sanfilippo et al., 2019). Hence, any estimate based on "DM-like" initial

280   composition furnishes an approximation of the overall degree of depletion of the actual upper

281   mantle composition that may depend by heterogeneities affected by old depletion events. As

282   a consequence, strongly refractory abyssal peridotites are not necessarily associated with

283   basalts formed at high melting degrees (Liu et al., 2008; Harvey et al., 2010; Salters et al.,

284   2011; Stracke et al., 2011). For instance, the very high F of the DFZ-N residual peridotites is

285   at odds with the geodynamic environment of a megatransform. Modelling subridge thermal

286   structure, Ligi et al. (2002, 2005) suggested that "constipated" magma production and low

287   degree of mantle melting (<5% at the ITR) are expected at ridge-transform intersection (RTI)

288   of transforms with exceptionally large (>30 Ma) age offset. This is due to a decrease in the

289   along-axis thermal gradient, which at the RTI may reach ~30°C/km at a depth of 20 km (Ligi

290   et al 2002). However, this strong reduction of the melting regime is not observed in the

291   basalts and peridotites from the northern sector of the Doldrums FZ that reveal moderate to

292   high degrees of partial melting (Fig. 1c). This may suggest that at the time of melting below

293   the MAR axis of these mantle peridotites, the former 600 km-long-offset Doldrums transform

294   was already segmented from the appearance of the intra-transform spreading segment

295   reducing the transform offset length and consequently the related cold edge effect. An

296   alternative explanation may be that some peridotites have preserved depleted characters

297   inherited by previous melting events (see Stracke et al, 2011; 2019; Mallick et al., 2015;

298   Sanfilippo et al., 2019);

299   *2)* the second assumption refers to the quantification of the residual character of abyssal

300   peridotites based on sp Cr#, i.e., mantle rocks did not suffer any post-melting process,

301   although these processes may slightly modify the sp Cr# without leaving obvious textural

302   evidence (see discussion in Hellebrand et al., 2002b; Warren et al., 2009; Warren, 2016). Due

303   to a much higher affinity with melt than to mantle peridotites, highly incompatible trace

304   elements (such as LILE and LREE) are sensitive proxies of melt-rock interactions and can be

305   used to obtain information on post-melting modifications. We modelled the REE composition

306   of cpx residual from fractional melting of DM mantle peridotites (Fig. 6). Aware of the

307   oversimplification based on the assumptions adopted, we used the depleted mantle (DM)

308   estimate of Salters and Stracke (2004) as common initial composition, using a fixed set of

309   REE partition coefficients from the same study. We used a dynamic melting model where

310   melting parameters (partition coefficients, melting coefficients and melting reaction) are

311   modified according to the decrease in pressure (from Longhi, 2000; Salters et al., 2002).

312   Critical porosity was fixed at 1%. Single melt increments, columnar melt and bulk residue

313   compositions were calculated separately. REE contents of residual cpx were derived from the

314   bulk composition following the equation $C_{(cpx)}=C_{(bulk)}*D_{(cpx)}/D_{(bulk)}$. Cpx in residual DFZ-N

315   peridotites have highly variable Yb contents relative to rather constant Dy/Yb and Sm/Yb

316   ratios (Figs. 7a and 7b). This requires the occurrence of garnet (grt) as buffer for HREE

317   during the first stages of melting (Johnson et al., 1990; Hellebrand et al., 2002; Brunelli et al.,

318   2006). Hence, we considered the possibility that melting might have started in the garnet

319   stability field, producing higher M-REE to H-REE fractionation and buffering Yb_N towards

320   high values (see also Stracke et al., 2011; Warren 2016). Results of the melting model are

321   shown in Figs. 6 and 7 suggesting that each sample lies on a different melting path. Overall,

322   our model indicates that cpx REE contents in DTF-N residual peridotites are reproduced by

323   an average degree of melting ranging from 10% to 14%, with a variable contribution of

324   garnet in the melting residue for the samples having the highest M-REE to H-REE

325   fractionations (S09-61/09 and S09-70/03; Figs. 7a and 7b). This estimate is slightly lower

326   than that based on the sp Cr#, but still higher than that based on Na_8 in associated basalts.

327   On closer inspection, however, only the M-REE to H-REE fractionation is somehow

328   reproduced by the model (Figs. 7a and 7b). Indeed, our model does not reproduce the

329   depletion in L-REE relative to M- and H-REE (Figs. 7c and 7d). This indicates that the L-

330   REE contents in these cpx are too high to be explained by the same process of near-fractional

331   melting that explains well the M- and H-REE concentrations. This feature is characteristic of

332   cpx in abyssal peridotites worldwide, of which L-REE diverge from partial melting trends as

333   shown in Fig. 7. However, this process can explain the M- and H-REE contents (compare

334   Figs.7a and 7b and Figs. 7c and 7d). Selective increases in highly incompatible relative to

335   less incompatible elements (such as LREE compared to M-and HREE) can be the effect of

336   post-melting modifications, such as entrapment of small aliquots of unextracted melt in the

337   asthenosphere (e.g., Brunelli et al., 2006; Seyler et al., 2007; Brunelli and Seyler, 2010) or the

338   chromatographic effect of reactive melt migration at lithospheric conditions (e.g., Godard et

339   al., 2008; Warren et al., 2009; Stracke et al., 2011). On this basis, Warren (2016) inferred that

340   interactions with melts after fractional melting affect abyssal peridotites worldwide.

341   We note that the cpx in DTF-N peridotites have suprachondritic $(La/Ce)_N$ ratios (Fig. 5)

342   often coupled to positive Sr anomalies. La and Sr have high affinity to seawater, so their

343   increase may also indicate contamination of the residual cpx by water-rich fluids. During the

344   LA-ICP-MS measurements, we accurately avoided microcracks or fluid inclusions. However,

345   given the extremely low La and Sr contents in residual cpx and the high serpentinization

346   degrees of our samples we cannot exclude that some enrichments in these elements may be

347   due to intracrystalline diffusion during serpentinization. Patterns with abrupt inversion of

348   LREE slope are not typical of abyssal peridotites, but have been reported in ultraslow mid-

349   ocean ridges such as the Gakkel Ridge (Hellebrand and Snow, 2003), the Southwest Indian

350   Ridge (Dantas et al., 2007) and the 15.20ºN fracture zone in the MAR (Seyler et al., 2006).

351   Seyler et al. (2006) suggested that the high La/Ce ratios were caused by incomplete

352   equilibration with melts percolating at low porosity and at extremely limited melt-rock ratio.

353   This would further support the idea of cryptic refertilization to account for the high L-REE

354   (Fig. 5a).

355   In summary, we infer that peridotites from DTF-N reveal moderate to high degrees of

356   partial melting, including a variable contribution of melting at garnet-facies conditions. Based

357   on the Na_8 variability of the basalts physically associated to the peridotites and on the

358   occurrence of these rocks along the transform wall of a long-lived fracture zone, we cannot

359   exclude that the refractory character was acquired during old melting events. Regardless of

360   age of depletion, melting was followed by a local enrichment in L-REE due to some

361   interactions with small amounts of melt that did not leave any visible textural evidence.

362

363   *6.2 Two stages of melt-rock reaction in the intra-transform domain: geochemical constraints*

364   The texture and composition of peridotites from the ITR and DTF-S suggest that these

365   rocks formed through interaction with percolating melts. In particular, we distinguished two

366   typologies of reacted peridotites: *i)* the pl-impregnated peridotites contain pl-opx veins; sp

367   have high Cr# and TiO_2 concentrations (Figs. 3a and 3b), and cpx display positive Ti-Na

368   correlation (Fig. 4a) and high M- and H-REE contents but depleted L-REE (Figs. 5a and 5c);

369   and *ii)* the refertilized peridotites show intergranular, fine-grained cpx, locally associated to

370   sp and pl. Sp Cr# is variable but always associated to low (<0.2 wt%) TiO_2 (Figs. 3a and 3b),

371   and cpx is rich in Na_2O and L-REE (Figs. 4a, 5a and 5d) but has TiO_2 and M- and H-REE

372   contents undistinguishable from those of residual peridotites.

373   Pl-peridotites are relatively common in the oceanic mantle at slow- and ultraslow-

374   spreading ridges. In the Atlantic, they are characteristic of the large transforms of the

375   equatorial region between Romanche and St Paul (Bonatti et al., 1996; Bonatti et al., 2001a,b;

376   Tartarotti et al., 2002, Brunelli and Seyler, 2010), as well as in the Kane transform (Dick et

377   al., 2008). Their occurrence can be related to crystallization and retention of melt at low

378   pressure and at high melt-rock ratio, due to a thick lithospheric lid. Pl crystallization

379   decreases the Al versus Cr contents in sp, cpx and opx (Dick, 1989) and generates Sr and Eu

380   depletions in cpx (Rampone et al., 1997), as well as modifications in incompatible elements

381 towards equilibrium with the interacting melt (see Piccardo et al., 2007). Based on this

382 rationale, cpx in pl-peridotites has been used to retrieve the composition of the migrating

383 melt. In our case, cpx are characterized by high H-REE contents, but depleted L-REE. These

384 incompatible element compositions are far from equilibrium with a MORB-type melt; they

385 suggest interaction with depleted melts. Hence, we can argue that a depleted, rather than

386 typical MORB-type melt, interacted with the residual peridotite to form pl-peridotites.

387 However, the reactive percolation of melt in a crystal matrix may cause modification in melt

388 composition and, hence, may give a biased estimate of the melt initially percolating in the

389 matrix. To gain insights into the original trace element composition (i.e., REE) of the melt

390 interacting with the residual mantle to produce the pl-impregnated peridotites, we need a

391 reactive porous flow numerical model, i.e., the non-dimensional "Plate Model" proposed by

392 Vernières et al. (1997). This model is able to reproduce the behaviour of trace elements

393 during melt–rock interactions in a rock-dominated system (porosity <20%; Vernières et al.,

394 1997). The Plate Model allows controlling elemental melt-mineral exchanges as porosity,

395 melt-rock ratio and crystallization degrees vary during the reaction, assuming local-

396 instantaneous equilibrium between phases (e.g., Godard et al., 1995; Vernières et al., 1997).

397 We model dissolution of a residual harzburgite by a percolating melt that subsequently

398 crystallizes ol, pl and cpx, assuming the following reaction:

399

400 $0.75\ Ol_m + 0.20\ Opx_m + 0.05\ Cpx_m + melt_p = 0.50\ Pl_c + 0.30\ Opx_c + 0.20\ Cpx_c + melt_r$ (1)
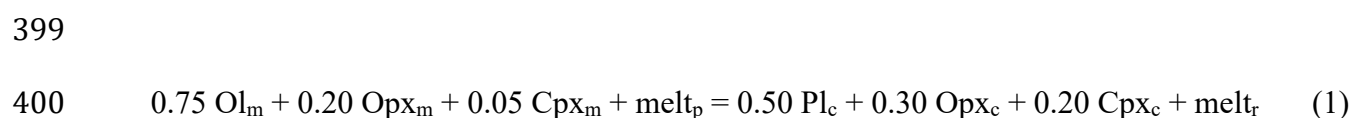
401

402 where Ol_m, Opx_m and Cpx_m are the mineral phases composing the former residual peridotite;

403 $melt_p$ is the percolating melt that triggers the reaction; Pl_c, Opx_c and Cpx_c are the minerals

404 produced by the reaction in equilibrium with the reacted melt ($melt_r$). Pl_c and Opx_c likely

405 crystallized from and Cpx_c re-equilibrated with the $melt_r$ during the reactive process.

406 Numbers in reaction (1) refer to the mineral proportions used in the model, while melt mass

407   vary as function of dissolution/precipitation extents (i.e., variation in porosity as reported in

408   Fig. 8a-c). Mineral proportions of products are estimated after textural observations (all

409   parameters of the model are reported in Supplementary Table 7).

410   The occurrence of pl-veins indicates high melt-rock ratios and high porosity in the

411   percolated rocks prior to the extensive crystallization and closure of the magmatic system.

412   We thereby simulate the melt reactive percolation process at increasing porosity (up to 5%

413   porosity) and, by consequence, increasing melt-rock ratio. We arbitrarily fixed initial porosity

414   at 1%. Bulk composition of the starting peridotite was re-calculated from the reference

415   composition of cpx in the residual peridotite from Peyve seamount (sample S06-63/38) using

416   the equation $C_{(bulk)} = C_{(cpx)} * D_{(bulk)} / D_{(cpx)}$, as proxy of the most refractory peridotite in the

417   studied area. We tested three compositions of the percolating melt (Fig. 8): a representative

418   N-MORB and two depleted melts.

419   First, we used the average N-MORB from the database of Gale et al. (2013) (Fig. 8a).

420   Given that, during melt transport and melt-rock interactions, H-REE move slower and change

421   steadily (Godard et al., 1995; Navon and Stolper, 1987; Vernières et al., 1997) while L-REE

422   move faster, the process produces strong enrichments in L-REE, which are quickly shifted

423   towards the composition of the migrating melt (Fig. 8a). Thus, models of reactive percolation

424   of an N-MORB with relatively high L-REE produce patterns not consistent with the cpx of

425   our pl-impregnated peridotites.

426   To account for the strong L-REE fractionation but rather high M-REE and H-REE

427   contents of cpx in the pl-impregnated peridotites, we assume the involvement of melts

428   depleted in L-REE compared to typical MORBs. This idea was advanced by several authors

429   to explain the occurrence of L-REE-depleted cpx in pl-bearing peridotites (Brunelli and

430   Seyler, 2010). Examples include L-REE-depleted cpx in pl-peridotites from the Alpine

431   (Rampone et al., 1997; 2008; Tribuzio et al., 2004; Piccardo et al., 2007; Guarnieri et al.,

432   2012; Sanfilippo et al., 2014; Basch et al., 2019), Othris (Dijkstra et al., 2003) and Bay of

433   Island (Suhr et al., 2003) ophiolites as well as St Paul transform (Brunelli and Seyler, 2010).

434   This hypothesis, however, involves the occurrence of "unaggregated" percolating melts,

435   which are expected to approach equilibrium with the residue. These melts correspond to the

436   incremental melts (hereafter 'single melt increments') produced by fractional melting of

437   mantle peridotites. Composition of these melts is assumed to equal the composition of the last

438   melt fraction generated at the shallowest pressure during continuous decompression partial

439   melting (i.e., Rampone et al., 1997; Seyler et al., 2006; Brunelli and Seyler, 2010). This

440   model requires no aggregation of such incremental melts in the asthenosphere, necessary for

441   the preservation of an extremely depleted character (Fig. 9a); any mixing with more enriched

442   melts would erase the depleted character, especially for the most incompatible elements

443   (Stracke and Burdon, 2009). An alternative explanation for the depleted percolating melts lies

444   in the occurrence of ultra-depleted melts produced by a refractory mantle source (Stracke et

445   al., 2019). These melts are not representative of single melt increments, but partly aggregated

446   melts from a refractory portion of the mantle. This inference is based on the idea that the

447   mantle asthenosphere preserves refractory portions not (or only partly) equilibrated after

448   ancient melting events (Harvey et al., 2006), and is mostly supported by the preservation of

449   old Re-depletion ages and extremely radiogenic Nd-Hf isotopic compositions in abyssal

450   peridotites (Liu et al., 2008; Stracke et al., 2011; Byerly and Lassiter, 2014; Mallick et al.,

451   2014; Mallick et al., 2015; Sanfilippo et al., 2019). Depending on the composition of this

452   refractory source, a resulting ultra-depleted melt (hereafter 'UD-Melt') would have M-REE

453   and H-REE contents similar to those of a single melt increment of a DM-like source, but with

454   substantially minor L-REE to M-REE fractionations (Fig. 9b).

455   Fig. 9 compares the composition of single melt increments due to fractional melting of a

456   common DM source at 5%, 10% (Fig. 9a), and ultra-depleted (UD) melts formed by 10%

457   melting of three refractory sources obtained as residuals after melting of the same DM source

458   (Fig. 9b). These melts were produced using the same dynamic melting model described

459   before. We hence performed the Plate Model using: *i)* a single melt increment produced by

460   5% melting of a DM source, having H-REE similar to cpx in pl-impregnated peridotites; and

461   *ii)* a UD-melt produced by 10% melting of a refractory source obtained after 10% melting of

462   a DM-mantle source, selected on the basis of L-REE contents and L-REE to M-REE

463   fractionations comparable to those of cpx in pl-impregnated peridotites. While both depleted

464   melts have H-REE approaching those of the cpx in our rocks, they have different L-REE

465   fractionations. Fig. 8b shows the results of the model using the single melt increment

466   compared to the cpx in the pl-impregnated peridotites. Since the L-REE contents of the

467   reactive percolating melt (i.e., single melt increment) are lower than that of the cpx in pl-

468   impregnated peridotites, the modelled cpx cannot reproduce the L-REE fractionation in our

469   rocks at given M-HREE contents. On the other hand, using the UD-melt, the modelled cpx

470   approaches the REE contents of our pl-impregnated peridotites.

471   The compositions of pl-impregnated peridotites are best modelled by impregnation of a

472   UD-melt produced by a refractory source (Fig. 8c), involving partial dissolution of a depleted

473   mantle harzburgite and precipitation of pl and opx (see reaction 1). In this scenario, cpx in pl-

474   impregnated peridotites represent the re-equilibrated porphyroclasts as products of reaction

475   when the system reaches 5% of interstitial melt (Fig. 8c). This is in agreement with the

476   occurrence of pl microveins and pl-opx patches covering ~5% volume. We note that only one

477   sample seems to be reproduced by our Plate Model. The parallel REE cpx patterns in the two

478   studied pl-impregnated rocks are associated with higher Ti contents and lower Mg# in the

479   cpx with the highest trace element contents (Fig. 8c). This suggests that a process of melt

480   fractionation, rather than further interaction with the matrix, formed the cpx with higher REE.

481   Therefore, the latter likely progressively modified the porphyroclasts, which re-equilibrated

482   with the melt residual after melt-rock interaction at decreasing melt mass during the closure

483   of the system.

484   If the pl-impregnated peridotites are produced by interaction with UD-melt, a melt with

485   strong depletion in L-REE relative to M-REE and H-REE appears to be at odd with the flat

486   REE pattern of the refertilized peridotites. The latter have very minor amount of pl in thin

487   section, and consistently show no Sr and Eu negative anomalies. One fundamental

488   observation is the finding of interstitial cpx in the refertilized peridotites. These cpx have

489   similar M-REE and H-REE but higher L-REE compared to the cpx porphyroclasts (Fig. 5d),

490   but almost undistinguishable major element compositions (Supplementary Tables 4 and 5).

491   This suggests that the melt crystallizing in the refertilized peridotites underwent a process of

492   re-equilibration and extensive crystallization at very low melt-rock ratio allowing the

493   preferential increase in highly incompatible LREE compared to the less compatible M-HREE

494   (see also Vernières et al., 1997; Piccardo et al., 2007; Basch et al., 2018). Hence, we infer that

495   the melt crystallizing the interstitial cpx in the refertilized peridotites percolated within a

496   crystal matrix at decreasing porosity, and without extensive assimilation of the crystal matrix.

497   Under these conditions, an interaction model using the reaction (1) to reproduce the pl-

498   impregnated peridotite would produce completely different results (see Vernières et al.,

499   1997). The least incompatible trace elements (such as M- and H-REE) are mainly controlled

500   by mineral reactions and are hence strongly buffered by the host peridotite (e.g., Godard et

501   al., 1995; Navon and Stolper, 1987), thereby resulting in M- and H-REE patterns controlled

502   mostly by the composition of the residual solid. On the other hand, the most incompatible

503   trace elements (L-REEs) are still controlled by local porosity and progressively buffered

504   towards high values by limited interaction with the percolating melt that, in the meantime,

505   decreases in mass as result of crystallization. This process results in the fractionation between

506   L-REE and M- and H-REE, producing L-REE contents even higher than those of the starting

507   melt (Piccardo et al., 2007). To reproduce the cpx of the refertilized peridotites we thereby

508   used the Plate Model set at low porosity (Fig. 8d), inhibiting the assimilation of the host rock

509   and decreasing the porosity until the closure of the system. Accordingly, we model the

510   following reaction:

511

512    $0.75\ Ol_m + 0.20\ Opx_m + 0.05\ Cpx_m + melt_p = 0.05\ Pl_c + 0.95\ Cpx_c + melt_r$ (2)
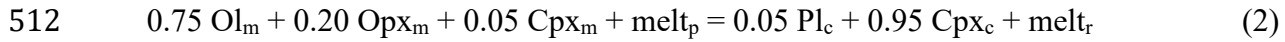
513

514   where Ol_m, Opx_m and Cpx_m are the mineral phases of the former residual peridotite (i.e.,

515   same starting material used to model the composition of pl-impregnated peridotite); $melt_p$ is

516   the percolating melt that triggers the reaction; Pl_c and Cpx_c are the minerals product of

517   reaction (i.e., crystallizing) in equilibrium with the reacted melt ($melt_r$). Mineral proportions

518   of crystallizing phases are estimated after textural observations (see details in Supplementary

519   Table 7).

520   We used the UD-melt modified by reaction (1) that has M- and H-REE similar to those of

521   cpx in the refertilized peridotites (green trend in Fig. 8c). Consistently, we set the initial

522   porosity at the porosity associated with this modified UD-melt (i.e., porosity = 3.5%; output

523   of modelled reaction 1). The results are satisfying (Fig. 8d), as we can reproduce the flat REE

524   patterns of the cpx in the refertilized peridotite starting with the same melt that produced the

525   pl-impregnated peridotites. The Plate Model results, together with the interstitial character of

526   cpx crystals, confirm that the cpx in the refertilized peridotite precipitated from the modified

527   UD-melt (by reaction 1) in low pororsity areas after reaction (2) at decreasing melt mass

528   (porosity <1%; Fig. 8d). The occurrence of UD-melt justifies the refractory character of these

529   rocks (low Ti, low H-MREE in cpx), whereas the interaction at low melt-rock ratio produced

530   enrichments in the most incompatible elements, like L-REE and Na.

531   In summary, the peridotites from the ITR and DTF-S experienced extensive percolation by

532   ultra-depleted melts. Our geochemical model suggests that these melts were produced by a

533   source with a more refractory composition compared to a typical DM-peridotite. The

534   percolating event probably occurred when the mantle section crossed the thermal boundary

535   layer entering in the cold lithosphere. High porosity (up to 5%), and thus high melt-rock ratio,

536   enhanced the formation of well-equilibrated pl-impregnated peridotites, whereas low melt-

537   rock ratios and decreasing porosity (from 3% porosity to <1%) explain the local occurrence

538   of refertilized pl-poor lithologies.

539

540   *6.3 Origin of the ultra-depleted melt*

541   Having established that a multiphase process of interaction of melts from a refractory

542   source is the best candidate to explain the geochemical variability of the peridotites from the

543   ITR and DTF-S of the Doldrums megatransform, we will now discuss the possible origin of

544   the ultra-depleted melts. Since the findings of old Re depletion ages in abyssal peridotites

545   from the 15º 20'N transform in the MAR (Harvey et al., 2006) and Gakkel ridge (Liu et al.,

546   2007), several authors have postulated that refractory portions of the mantle may survive

547   from stirring and equilibration in the asthenosphere, thus representing a hidden component in

548   the upper mantle (see also Stracke et al., 2011; Byerly and Lassiter, 2014). The recent

549   conception of the upper mantle is of a heterogeneous asthenosphere with a depleted matrix,

550   i.e., formed by variably depleted peridotites mixed with enriched lithologies, i.e., re-fertilized

551   peridotites or pyroxenites (e.g., Liu et al., 2008; Stracke et al., 2019; Sanfilippo et al., 2019).

552   Melting such a heterogeneous mantle would decrease preferentially the amount of enriched

553   lithologies, in turn resulting in a higher overall contribution of the most depleted end

554   members. As a result, after the production of new oceanic crust, the mantle emplaced in the

555   oceanic lithosphere is more depleted than the asthenosphere. We infer that the opening of an

556   intra-transform domain may cause these depleted portions of oceanic upper mantle to melt a

557   second time, until new asthenosphere is emplaced in the shallower portions of the melting

558   column. To assess the ability of ultra-depleted mantle to generate significant quantities of

559   melt, we used *pMELTS* software (Ghiorso et al., 2002) and model the adiabatic ascent and

560   melting of mantle with different compositions. The starting compositions are refractory

561   sources obtained after 5% and 10% melting of a DM-mantle (Workman and Hart, 2005).

562   These sources were subjected to adiabatic decompression (adiabatic thermal gradient of

563   0.8°C/km) from 15 kbar to 5 kbar, adopting different mantle potential temperatures (Tp =

564   1375°C, 1350°C and 1325°C at 15 kbar). The results are shown in Fig. 10, where melt

565   productivity as a function of pressure indicates that these sources are sufficiently fertile to

566   generate significant quantities of melt. In particular, assuming a typical mantle potential

567   temperature of ~1350 °C, an ultra-depleted mantle residual after 10% melting will still

568   generate up to 10% melt by 5 kbar, which approximate the base of the lithosphere in a

569   transform domain (Ligi et al., 2005). It is therefore plausible that the ultra-depleted melts

570   refertilizing the Doldrums peridotites formed by re-melting of a residual mantle originally

571   melted at the ridge axis and intercepted by the mantle raising to the ITR axis while flowing

572   away parallel to the transform.

573   A detailed geochemical characterization of the basalts from the ITR is still not available.

574   Nonetheless, minor and trace elements data from some basalts in the region are reported in

575   the cruise report of Expeditions S06 and S09 (Skolotnev et al., 1991). These preliminary data

576   indicate that the basalts spatially associated with the ITR peridotites have a N-MORB-type

577   geochemical signature. There seems to be no evidence for trace elements depleted melts

578   amongst the erupted magmas. We emphasize, however, that erupted MORBs are mixtures of

579   melts from a heterogeneous source, and any melt with an ultra-depleted composition would

580   readily loose its depleted character after mixing with melts deriving from more enriched

581   counterparts (e.g., Stracke and Burdon, 2009; Salters et al., 2011). For this reason, the

582   contribution of a refractory source remains unseen in erupted MORBs without combining

583   trace element compositions with Nd-Hf isotopic ratios (Salters et al., 2011; Stracke et al.,

584   2011; 2019; Sanfilippo et al., 2019). Hence, even if ultra-depleted melts were produced

585   within the intra-transform domain, their contribution to the trace element contents of the

586   erupted melts is not observed.

587   A remaining issue is why the mantle peridotites record exclusively the interaction with

588   such ultra-depleted melts, whereas peridotites pervaded by more enriched melts are not

589   observed. Owing to its refractory character, an ultra-depleted mantle would start melting at

590   lower pressures compared to a more fertile peridotite, and ultra-depleted melts are thereby

591   expected to be the shallower products of the melting column. For instance, our *pMELTS*

592   thermodynamic models show that a refractory peridotite residual after by ~10% melting of a

593   DM source would start melting at a pressure of 0.7 GPa for a mantle potential temperature of

594   ~1350ºC (Fig. 10b), compared to the >2.5 GPa of a peridotite with a DM-like composition.

595   Hence, the migration of these late-stage melts in the lithospheric lid would have occurred

596   soon after their formation. The sub-axial cold regime and the thick lithosphere characteristic

597   of ridge segments offset by slow-slip long-offset transforms (Ligi et al., 2002) might have

598   further enhanced a diffuse melt migration mechanism, increasing the potential to interact and

599   crystallize within the mantle peridotites (Niu, 2004). On the contrary, melts formed at greater

600   depth in the melting region and, thus, produced from more fertile domains, might have been

601   focused into high permeability channels precluding interaction with the ambient peridotite

602   (Spiegelman and Kelemen, 2003; Liang and Parmentier, 2009; Lambart et al., 2009;

603   Sanfilippo et al., 2017). Melt-impregnated peridotites with a characteristic depleted

604   composition are indeed widely reported in mantle sections related to cold thermal regimes

605   such as the intra-transform domains of the St Paul transform system (Brunelli and Seyler,

606   2010) or the mantle section of the Jurassic Alpine ophiolites (Rampone et al., 2008; Guarnieri

607   et al., 2012; Sanfilippo et al., 2019; Basch et al., 2019). The impregnated peridotites from the

608   ITR domain of the Doldrums transform system may thereby represent a snapshot of the

609   process of pervasive migration of ultra-depleted melts through a thick lithospheric mantle,

610   before they mix with more enriched melts at shallower levels.

611

612

7. Conclusions

The Doldrums MTS domain reveals a multistage tectonic evolution resulting in a large age-offset multi-faults transform system. Tectonic forces active in this complex system led to the exhumation of mantle rocks at different locations along the megatransform system, including the northernmost transform (Doldrums) and intra-transform ridge segment (ITR-1). Peridotites from the northern wall of the Doldrums transform valley suffered variable degrees of melt extraction, which left a residual solid deprived of highly incompatible elements and limited evidence for late-stage interaction with migrating melts. Based on geochemical models, we infer that this residual mantle suffered moderate to high degrees of mantle melting (10 to 14% based on REE modelling), with some contribution of melting (likely <5 %) in the garnet-stability field. In the intra-transform domain the refractory peridotites show textural and chemical evidence for interactions with migrating melts. Two typologies of reacted rocks have been identified: pl-impregnated and refertilized peridotites. The pl-impregnated peridotites formed at high porosity and high melt-rock ratio, conditions that allowed complete re-equilibration of the original mantle minerals with the interacting melt. Refertilized peridotites were instead generated under highly reduced porosity, when small fractions of the impregnating melt were trapped within the mantle matrix. Geochemical models imply a depleted reacting melt, produced by a mantle highly depleted in incompatible elements that probably experienced previous melt extraction events below the ridge axis, before being then transposed laterally parallel to the transform. Once ITR-1 has formed, this refractory mantle, intercepted by the raising mantle below the ITR axis, may melt a second time, producing ultra-depleted melts.

643

References

645   Anders, E., Grevesse, N., 1989. Abundances of the elements: Meteoritic and solar. Geochimica
646   et Cosmochimica Acta, 53, 197–214.

647   Basch, V., Rampone, E., Borghini, G., Ferrando, C., Zanetti, A., 2019. Origin of pyroxenites in
648   the oceanic mantle and their implications on the reactive percolation of depleted melts.
649   Contributions to Mineralogy and Petrology 174, 97. https://doi.org/10.1007/s00410-019-
650   1640-0.

651   Basch, V., Rampone, E., Crispini, L., Ferrando, C., Ildefonse, B. & Godard, M., 2018. From
652   mantle peridotites to hybrid troctolites: textural and chemical evolution during melt–rock
653   interaction history (Mt. Maggiore, Corsica, France). Lithos, 323, 4-23.
654   https://doi.org/10.1016/j.litho s.2018.02.025

655   Bonatti, E., Ligi, M., Brunelli, D., Cipriani, A., Fabretti, P., Ferrante, V., Gasperini, L., Ottolini,
656   L., 2003. Mantle thermal pulses below the Mid-Atlantic Ridge and temporal variations in
657   the formation of oceanic lithosphere. Nature 423, 499–505.

658   Bonatti, E., Brunelli, D., Fabretti, P., Ligi, M., Portaro, R.A., Seyler, M.,2001. Steady-state
659   creation of crust-free lithosphere at cold spots in mid-ocean ridges. Geology 29, 979–982.

660   Bonatti, E., Ligi, M., Carrara, G., Gasperini, L., Turko, N., Perfiliev, S., Peyve, A., Sciuto, P.F.,
661   1996. Diffuse impact of the Mid-Atlantic Ridge with the Romanche transform: an ultracold
662   ridge-transform intersection. Journal of Geophysical Research: Solid Earth 101(B4), 8043–
663   8054.

664   Byerly, B. L., Lassiter, J. C., 2014. Isotopically ultradepleted domains in the convecting upper
665   mantle: implications for MORB petrogenesis. Geology 42, 203–206.

666   Brunelli, D., Ligi, M., Bonatti, E., Cipriani, A., 2019. Melting-induced fluctuations on the
667   shallow thermal regime at the Vema transform, Mid Atlantic Ridge. In *Geophysical
668   Research Abstracts* (Vol. 21).

669   Brunelli, D., Cipriani, A., Bonatti, E., 2018. Thermal effects of pyroxenites on mantle melting
670   below mid-ocean ridges. *Nature Geoscience*, *11*(7), 520–525.

671   Brunelli, D., Seyler, M., 2010. Asthenospheric percolation of alkaline melts beneath the St. Paul
672   region (Central Atlantic Ocean). Earth and Planetary Science Letters 289, 393–405.

673   Brunelli, D., Seyler, M., Cipriani, A., Ottolini, L., Bonatti, E., 2006. Discontinuous melt
674   extraction and weak refertilization of mantle peridotites at the Vema lithospheric section
675   (Mid-Atlantic Ridge). Journal of Petrology 47, 745–771.

Dick, H.J., Lissenberg, C.J., Warren, J.M., 2010. Mantle melting, melt transport, and delivery beneath a slow-spreading ridge: The paleo-MAR from 23 15′ N to 23 45′ N. Journal of Petrology 51, 425–467.

Dick, H.J., Tivey, M.A., Tucholke, B.E., 2008. Plutonic foundation of a slow-spreading ridge segment: Oceanic core complex at Kane Megamullion, 23 30′ N, 45 20′ W. Geochemistry, Geophysics, Geosystems 9.

Dick, H.J.B., 1989. Abyssal peridotites, very slow spreading ridges and ocean ridge magmatism. Geological Society, London, Special Publications 42, 71–105.

Dick, H.J., Bullen, T., 1984. Chromian spinel as a petrogenetic indicator in abyssal and alpine-type peridotites and spatially associated lavas. Contributions to Mineralogy and Petrology 86, 54–76.

Dijkstra, A.H., Barth, M.G., Drury, M.R., Mason, P.R., Vissers, R.L., 2003. Diffuse porous melt flow and melt-rock reaction in the mantle lithosphere at a slow-spreading ridge: A structural petrology and LA-ICP-MS study of the Othris Peridotite Massif (Greece). Geochemistry, Geophysics, Geosystems 4.

Ferrando, C., Godard, M., Ildefonse, B. & Rampone, E., 2018. Melt transport and mantle assimilation at Atlantis Massif (IODP Site U1309): constraints from geochemical modelling. Lithos, 323, 24–43.

Gale, A., Dalton, C.A., Langmuir, C.H., Su, Y., Schilling, J.G., 2013. The mean composition of ocean ridge basalts. Geochemistry, Geophysics, Geosystems 14, 489–518.

Ghiorso, M.S., Hirschmann, M.M., Reiners, P.W., Kress, V.C. III (2002) The pMELTS: A revision of MELTS aimed at improving calculation of phase relations and major element partitioning involved in partial melting of the mantle at pressures up to 3 GPa. Geochemistry, Geophysics, Geosystems 3(5), doi: 10.1029/2001GC000217

Godard, M., Bodinier, J.-L., Vasseur, G., 1995. Effects of mineralogical reactions on trace element redistributions in mantle rocks during percolation processes: a chromatographic approach. Earth and Planetary Science Letters 133, 449–461. https://doi.org/10.1016/0012-821X(95)00104-K.

Guarnieri, L., Nakamura, E., Piccardo, G.B., Sakaguchi, C., Shimizu, N., Vannucci, R., Zanetti, A., 2012. Petrology, trace element and Sr, Nd, Hf isotope geochemistry of the North Lanzo peridotite massif (Western Alps, Italy). Journal of Petrology 53, 2259–2306.

Hellebrand, E., Snow, J. E., 2003. Deep melting and sodic metasomatism underneath the highly oblique-spreading Lena Trough (Arctic Ocean). Earth and Planetary Science Letters 216, 283–299.

Hellebrand, E., Snow, J. E., Hoppe, P., Hoffmann, A. W., 2002. Garnet-field melting and late-stage refertilization in 'residual' abyssal peridotites from the Central Indian Ridge. Journal of Petrology 43, 2305–2338.

Hellebrand, E., Snow, J. E., Dick, H. J., Hofmann, A. W., 2001. Coupled major and trace elements as indicators of the extent of melting in mid-ocean-ridge peridotites. Nature, 410(6829), 677–681.

Harvey, J., Gannoun, A., Burton, K.W., Rogers, N.W., Alard, O., Parkinson, I.J., 2006. Ancient melt extraction from the oceanic upper mantle revealed by Re–Os isotopes in abyssal peridotites from the Mid-Atlantic ridge. Earth and Planetary Science Letters 244, 606–621.

Kelemen, P., Kikawa, E., Miller, D. J., et al., 2004. ODP Leg 209 drills into mantle peridotite along the Mid-Atlantic Ridge from 14 N to 16 N. Proceedings of the Ocean Drilling Program, Initial Reports, 209: College Station, TX (Ocean Drilling Program).

Kelemen, P.B., Whitehead, J.A., Aharonov, E., Jordahl, K.A., 1995. Experiments on flow focusing in soluble porous media, with applications to melt extraction from the mantle. Journal of Geophysical Research: Solid Earth 100, 475–496.

Klein, E. M., & Langmuir, C. H., 1987. Global correlations of ocean ridge basalt chemistry with axial depth and crustal thickness. Journal of Geophysical Research: Solid Earth, 92(B8), 8089-8115.

Lambart, S., Laporte, D., Schiano, P., 2009. An experimental study of focused magma transport and basalt–peridotite interactions beneath mid-ocean ridges: implications for the generation of primitive MORB compositions. Contributions to Mineralogy and Petrology 157, 429–451.

Liang, Y., Parmentier, E.M., 2010. A two-porosity double lithology model for partial melting, melt transport and melt–rock reaction in the mantle: mass conservation equations and trace element transport. Journal of Petrology 51, 125–152.

Ligi, M., Bonatti, E., Cipriani, A., Ottolini, L., 2005. Water-rich basalts at mid-ocean-ridge cold spots. Nature 434, 66–69.

Ligi, M., Bonatti, E., Gasperini, L., Poliakov, A.N., 2002. Oceanic broad multifault transform plate boundaries. Geology 30, 11–14.

Liu, B., Liang, Y., 2017. The prevalence of kilometer-scale heterogeneity in the source region of MORB upper mantle. Science Advances 3(11), e1701872.

Liu, C.-Z., Snow, J.E., Hellebrand, E., Brügmann, G.E., von der Handt, A.B., Hofmann, A.W., 2008. Ancient, highly heterogeneous mantle beneath Gakkel ridge, Arctic Ocean. Nature 452, 311–316.

Longhi, J., 2002. Some phase equilibrium systematics of lherzolite melting: I. Geochemistry, Geophysics, Geosystems 3, 1–33.

Maia, M., Sichel, S., Briais, A., Brunelli, D., Ligi, M., Ferreira, N., Campos, T., Mougel, B., Brehme, I., Hémond, C., Motoki, A., Moura, D., Scalabrin, C., Pessanha, I., Alves, E., Ayres, A. & Oliveira, P., 2016. Extreme mantle uplift and exhumation along a transpressive transform fault. Nature Geoscience, 9(8), 619-623.

Mallick, S., Standish, J. J., & Bizimis, M., 2015. Constraints on the mantle mineralogy of an ultra-slow ridge: hafnium isotopes in abyssal peridotites and basalts from the 9–25 E Southwest Indian Ridge. Earth and Planetary Science Letters, 410, 42-53.

Mallick, S., Dick, H.J., Sachi-Kocher, A., Salters, V.J., 2014. Isotope and trace element insights into heterogeneity of subridge mantle. Geochemistry, Geophysics, Geosystems 15, 2438–2453.

Navon, O., Stolper, E., 1987. Geochemical consequences of melt percolation: the upper mantle as a chromatographic column. Journal of Geology 95, 285–307.

Niu, Y., 2004. Bulk-rock major and trace element compositions of abyssal peridotites: implications for mantle melting, melt extraction and post-melting processes beneath mid-ocean ridges. Journal of Petrology 45, 2423–2458.

Piccardo, G.B., Vissers, R.L. M., 2007. The pre-oceanic evolution of the Erro-Tobbio peridotite (Voltri Massif, Ligurian Alps, Italy). Journal of Geodynamics 43, 417–449.

Piccardo, G.B., Zanetti, A., Müntener, O., 2007. Melt/peridotite interaction in the Southern Lanzo peridotite: field, textural and geochemical evidence. Lithos 94, 181–209.

Pushcharovsky, Yu.M., Raznitsin, Yu.N., Mazarovich, A.O., Skolotnev, S.G., Kepezinskas, P.K., Tyrko, N.N., Peyve, A.A. and Dmitriev, D.A., 1992. Fracture zones Arkhangelsky, Doldrums and Vernadsky in the Central Atlantic: structure and rocks composition. Geotectonika 6, 63–79 (in Russian).

Pushcharovsky Yu.M., Raznitsin Yu.N., Mazarovich A.O. et al., 1991. Structure of the Doldrums fracture zone Central Atlantic. M. Nauka, pp. 224 (in Russian).

Pushcharovsky, Y.M., Peyve, A.A., Raznitsin, Y.N., Skolotnev, S.G., Lyapunov, S.M., Tyrko, N.N., 1988. Cape Verde Fracture Zone: Rock composition and structures (central Atlantic). Geotektonika 6, 18–31.

Rampone, E., Piccardo, G. B., & Hofmann, A.W., 2008. Multi-stage melt–rock interaction in the Mt. Maggiore (Corsica, France) ophiolitic peridotites: microstructural and geochemical evidence. Contributions to Mineralogy and Petrology 156, 453–475.

Rampone, E., Piccardo, G.B., Vannucci, R., Bottazzi, P., 1997. Chemistry and origin of trapped melts in ophiolitic peridotites. Geochimica et Cosmochimica Acta 61, 4557–4569.

Salters, V.J., Mallick, S., Hart, S.R., Langmuir, C.E., Stracke, A. (2011). Domains of depleted mantle: New evidence from hafnium and neodymium isotopes. Geochemistry, Geophysics, Geosystems 12, Q08001. doi:10.1029/2011GC003617.

Salters, V.J., Stracke, A., 2004. Composition of the depleted mantle. Geochemistry, Geophysics, Geosystems 5, Q05B07. doi:10.1029/2003GC000597.

Salters, V.J., Longhi, J.E., Bizimis, M., 2002. Near mantle solidus trace element partitioning at pressures up to 3.4 GPa. Geochemistry, Geophysics, Geosystems 3, 1-23. doi:10.1029/2001GC000148.

Sanfilippo, A., Salters, V., Tribuzio, R., Zanetti, A., 2019. Role of ancient, ultra-depleted mantle in Mid-Ocean-Ridge magmatism. Earth and Planetary Science Letters 511, 89–98.

Sanfilippo, A., Tribuzio, R., Ottolini, L., Hamada, M., 2017. Water, lithium and trace element compositions of olivine from Lanzo South replacive mantle dunites (Western Alps): new constraints into melt migration processes at cold thermal regimes. Geochimica et Cosmochimica Acta 214, 51–72.

Sanfilippo, A., Tribuzio, R., Tiepolo, M., 2014. Mantle–crust interactions in the oceanic lithosphere: Constraints from minor and trace elements in olivine. Geochimica et Cosmochimica Acta 141, 423–439.

Seyler, M., Lorand, J.P., Dick, H.J., Drouin, M., 2007. Pervasive melt percolation reactions in ultra-depleted refractory harzburgites at the Mid-Atlantic Ridge, 15 20′ N: ODP Hole 1274A. Contributions to Mineralogy and Petrology 153, 303.

Seyler, M., Lorand, J.P., Toplis, M.J., Godard, G., 2004. Asthenospheric metasomatism beneath the mid-ocean ridge: Evidence from depleted abyssal peridotites. Geology 32, 301–304.

Seyler, M., Toplis, M.J., Lorand, J.P., Luguet, A., Cannat, M., 2001. Clinopyroxene microtextures reveal incompletely extracted melts in abyssal peridotites. Geology 29, 155–158.

804   Seyler, M., Bonatti, E., 1997. Regional-scale melt-rock interaction in lherzolitic mantle in the
805   Romanche Fracture Zone (Atlantic Ocean). Earth and Planetary Science Letters, 146, 273–
806   287.

807   Sclater J.G., Grindlay N.R., Madsen J.A., Rommevaux-Jestin C., 2005. Tectonic interpretation
808   of the Andrew Bain transform fault: Southwest Indian Ocean. Geochemistry, Geophysics,
809   Geosystems 6, Q09K10, doi:10.1029/2005GC000951.

810   Suhr, G., Kelemen, P., Paulick, H., 2008. Microstructures in Hole 1274A peridotites, ODP Leg
811   209, Mid-Atlantic Ridge: Tracking the fate of melts percolating in peridotite as the
812   lithosphere is intercepted. Geochemistry, Geophysics, Geosystems 9, Q03012,
813   doi:10.1029/2007GC001726.

814   Suhr, G., Hellebrand, E., Snow, J.E., Seck, H.A., 2003. Significance of large, refractory dunite
815   bodies in the upper mantle of the Bay of Islands Ophiolite. Geochemistry, Geophysics,
816   Geosystems 4, 8605, doi:10.1029/2001GC000277.

817   Skolotnev, S.G., Sanfilippo, A., Peyve, A., Muccini, F., Sokolov, S.Y., Sani, C., Dobroliubova,
818   K.O., Ferrando, C., Chamov, N.P., Palmiotto, C., Pertsev, A.N., Bonatti, E., Cuffaro, M.,
819   Gryaznova, A.C., Sholukhov, K.N., Bich, A.S., Ligi., M., 2020. Large-scale structure of the
820   Doldrums multi-fault transform system (7-8º N Equatorial Atlantic): preliminary results
821   from the 45th expedition of the R/V A.N. Strakhov. Ofioliti 45, 25–41.

822   Skolotnev, S.G., Peyve, A.A., Turko, N.N., Tsukanov, N.V., Golovina, L.A., Efimov, V.N.,
823   Eskin, A.E., Lavrushin, V.Yu., Petrova, V.V., Chaplygina, N.L., 2006, February. New data
824   on the geological structure of the junction between the Cape Verde Seamount and the Cape
825   Verde Basin, central Atlantic. Doklady Earth Sciences 407(1), 220–224.

826   Skolotnev, S. G., Raznitsin, Yu. N., Mazarovich, A. O. et al., 1991. In Pushcharovsky, Yu. M.
827   (Ed.), *Structure* of the *Doldrums Fracture Zone*: *Central Atlantic*, Nauka, Moscow, 34–143.

828   Spiegelman, M., Kelemen, P.B., 2003. Extreme chemical variability as a consequence of
829   channelized melt transport. Geochemistry, Geophysics, Geosystems 4(7), 1055,
830   doi:10.1029/2002GC000336.

831   Stracke, A., Genske, F., Berndt, J., Koornneef, J.M., 2019. Ubiquitous ultra-depleted domains in
832   Earth's mantle. Nature Geoscience 12(10), 851–855.

833   Stracke, A., Snow, J.E., Hellebrand, E., Von Der Handt, A., Bourdon, B., Birbaum, K., Günther,
834   D., 2011. Abyssal peridotite Hf isotopes identify extreme mantle depletion. Earth and
835   Planetary Science Letters 308(3-4), 359–368.

836   Stracke, A., Bourdon, B., 2009. The importance of melt extraction for tracing mantle
837   heterogeneity. Geochimica et Cosmochimica Acta 73(1), 218–238.

838   Tartarotti, P., Susini, S., Nimis, P., Ottolini, L., 2002. Melt migration in the upper mantle along
839   the Romanche Fracture Zone (Equatorial Atlantic). Lithos 63(3-4), 125–149.

840   Tribuzio, R., Thirlwall, M.F., Vannucci, R., 2004. Origin of the gabbro–peridotite association
841   from the Northern Apennine Ophiolites (Italy). Journal of Petrology 45(6), 1109–1124.

842   Vernières, J., Godard, M., Bodinier, J.L., 1997. A plate model for the simulation of trace element
843   fractionation during partial melting and magma transport in the Earth's upper mantle.
844   Journal of Geophysical Research: Solid Earth 102, 24771–24784.

845   Warren, J. M., 2016. Global variations in abyssal peridotite compositions. Lithos 248, 193–219.

846 Warren, J.M., Shimizu, N., 2010. Cryptic variations in abyssal peridotite composition: evidence
847   for recent melt–rock reaction at the ridge. Journal of Petrology 51, 395–423.

848 Warren, J.M., Shimizu, N., Sakaguchi, C., Dick, H.J.B., Nakamura, E., 2009. An assessment of
849   upper mantle heterogeneity based on abyssal peridotite isotopic compositions. Journal of
850   Geophysical Research 114, B12203. https://doi.org/10.1029/2008JB006186.

851 Wilson, J.T., 1965. A new class of faults and their bearing on continental drift. Nature
852   207(4995), 343–347.

853 Workman, R.K., Hart, S.R., 2005. Major and trace element composition of the depleted MORB
854   mantle (DMM). Earth and Planetary Science Letters 231, 53–72.

855
856

857

Figure captions

Figure 1. Bathymetry of the equatorial Mid Atlantic Ridge region (a) morpho-structural

setting of the Doldrums transform system. White dashed box refers to the area displayed in **b**.

(b) Multibeam bathymetry of the northern sector of the Doldrums transform system from

Skolotnev et al. (2020) including dredging sites (filled circles). Colours identify dredges from

different locations of the transform domain. DTF-North and DTF-South indicate dredges from

the northern and southern walls of the northernmost transform valley (Doldrums transform),

respectively; ITR-1 indicates dredges from the central sector of the northernmost intra-

transform ridge segment. (c) Na_8 contents (i.e., NaO calculated at 8wt% MgO, after Klein and

Langmuir, 1987) of basalts collected during expeditions S06 and S09 and associated to the

studied peridotites. Average values and relative standard deviations are indicated for each

dredge station. Original values in Skolotnev et al. (1991).

Figure 2. Microphotographs showing the main petrographical features of the Doldrums

peridotites (a-b, residual peridotites; c-d, plagioclase-impregnated peridotite; e-f, refertilized

peridotite). (a) cross-polarized image showing a large, partly deformed porphyroclastic

orthopyroxene (opx) mantled by opx neoblasts, and embedded in a matrix of completely

serpentinized olivine (sample S06-61/9); (b) large, deformed clinopyroxene (cpx) in contact

with small clusters of neoblastic cpx (sample S09-70/03); (c) representative example of

plagioclase (pl) and opx-rich veins (sample S09-69/57); (d) detail of well-equilibrated textures

and triple junctions between pl and opx shown in **c** (sample S09-69/57); (e) association of

small, pl grains and interstitial cpx around a large porphyroclastic opx (sample S09-69/15); (f)

example of an intergrowing between Cr-spinel (sp) with irregular, lobate shape and interstitial

cpx (sample S09-69/02).

882

Figure 3. Covariations of spinel Mg#[Mg/(Mg+Fe)] (a), spinel TiO_2 (wt%) (b), olivine

forsterite (Fo mol%) (c) and clinopyroxene TiO_2 (wt%) (d) versus spinel Cr#[Cr/(Cr+Al)] of

the Doldrums peridotites. A compilation of residual and veined abyssal peridotites are from

Warren (2016). The chemical trends of partial melting (black-dashed arrow) and melt-rock

reaction (grey-dashed arrow) are also traced. DM compositions from Salters and Stracke

(2004). The colours of the symbols recall the position of each dredge along the fracture zone

as shown in Fig. 2a. Degree of mantle melting (F%) based on the sp Cr# following Hellebrand

et al. (2002).

Figure 4. Covariations of Cr# in cpx and opx (a) and of Na_2O versus TiO_2 in cpx of Doldrums

peridotites. Refertilized peridotites and pl-impregnated rocks are also indicated. Symbols as in

Fig. 3.

Figure 5. Chondrite-normalized incompatible trace elements concentrations (a) and REE (b-d)

of cpx from Doldrums peridotites. Note that REE patterns define three distinct cpx

compositions corresponding to the different structural setting of dredge locations. Symbol as

in Fig. 3. Colors as indicated for samples locations.

Figure 6. Dynamic melting model the REE composition of a residual cpx (black lines)

produced by process of near-fractional melting ($F = 0$-14%) starting from a DM composition

from Salters and Stracke (2004) and using melting equations and a constant set of partition

coefficients from the same study. Dashed lines represent melting in the spinel field (red), 3.5%

melting in the garnet followed by further 10.5% melting in the spinel fields (green), 5%

melting in the garnet followed by further 9% melting in the spinel fields (blue). Each step

represents 2% melting.

Figure 7. Variations of (Gd/Yb)$_N$, (Sm/Yb)$_N$, (Ce/Sm)$_N$ and (Ce/Yb)$_N$ versus Yb$_N$ (chondrite-

normalized) in cpx from Doldrums peridotites compared with the fractional melting models

shown in Fig. 6. Stars indicate the starting composition (DM, Salters and Stracke, 2004). Each

fractional melting trend is depicted in red, green and blue as in Fig. 6. Each step represents

0.2% melting. A compilation of residual abyssal peridotites from Warren (2016) is also shown

for comparison.
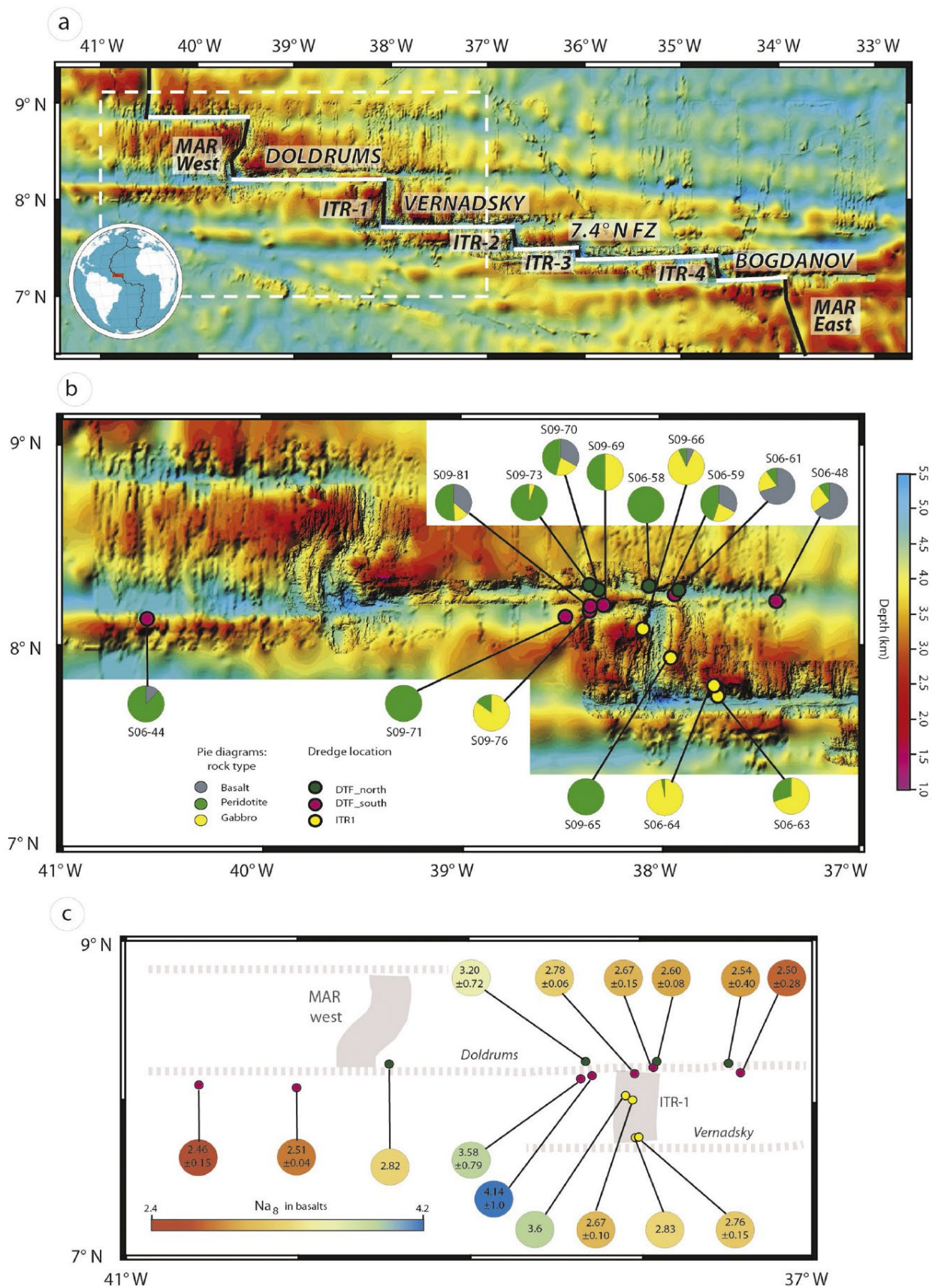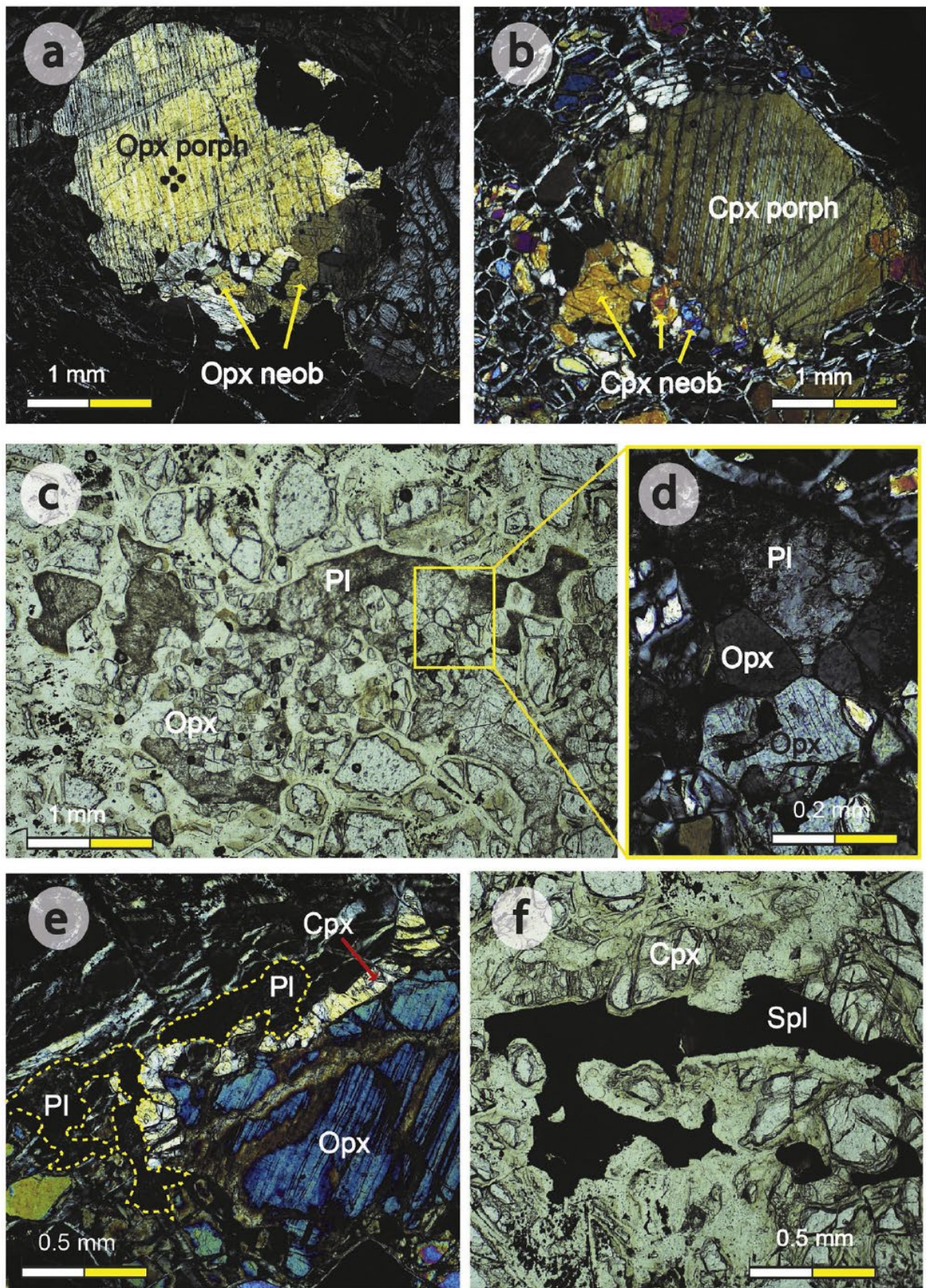
915

Figure 8. Chondrite-normalized REE contents in cpx from pl-impregnated peridotites (a, b, c) and refertilized peridotites (d) compared to cpx compositions modelled by reactive percolation through a residual peridotite (see text for details on starting rock composition) using the non-dimensional Plate Model by Vernières et al. (1997). Red curve: cpx in starting residual peridotite; Blue curve: cpx in equilibrium with percolating melt; Black-thick curves: cpx in pl-impregnated peridotite and refertilized peridotite; Black-dotted-thin curves: cpx in equilibrium with reacted melts from single increments of the Plate Model. (a), (b), (c) Models of peridotite pl-impregnation at high melt-rock ratios; reaction is set at increasing porosity (from 1 to 5% as reaction proceeds; values are reported on the left of modelled curves) using three melt compositions (see text for details on the choice of melts): (a) average N-MORB (Gale et al., 2013), (b) single melt increment after 8% fractional melting of a DM mantle source (Workman and Hart, 2005), and (c) ultra-depleted melt produced by 10% melting a refractory source in turn residual after 10% melting from of a DM-mantle. (d) Models of peridotite refertilization at low melt-rock ratio; reaction is set at decreasing porosity (i.e., melt mass; values are reported on the left of modelled curves) using a reacted melt from the impregnation process (green-dotted curve). Ol, cpx, opx and pl partition coefficients are those used by Ferrando et al. (2018).

Figure 9. Comparison between CI-normalized REE composition of ultra-depleted melts formed as (a) single melt increments extracted after 5 and 10% of partial melting from a common DM source; (b) aggregated melts produced by 10% melting of refractory sources (solid lines), in turn residual after 5 and 10% partial melting (dashed lines). These refractory sources are calculated as average compositions of a triangular melting region produced by 5 and 10% partial melting of a DM mantle. Melting model as in Fig. 8.
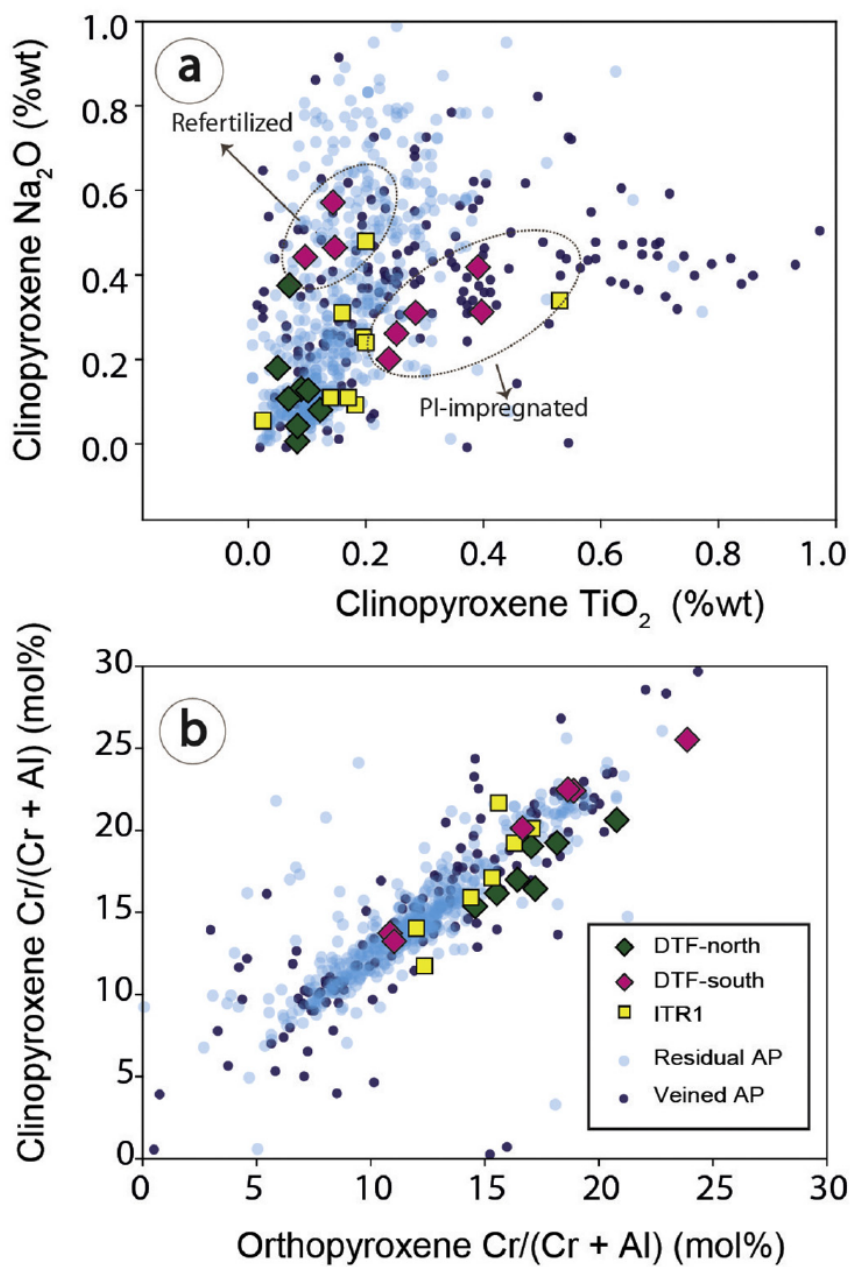
Figure 10. Melt fraction (%) vs pressure produced during adiabatic decompression and melting of a ultra-depleted mantle with different compositions. DM-5% and DM-10% correspond to DM mantle composition (Workman and Hart, 2005) residual after 5% and 10% adiabatic melting, respectively. We considered an adiabatic thermal gradient of 0.8°C/km along the decompression path from 15 to 5 kbar. The gradual blue background represents the progressive incorporation of depleted mantle portions in the thermal boundary layer upon decompression (at 5 kbar).

952
953
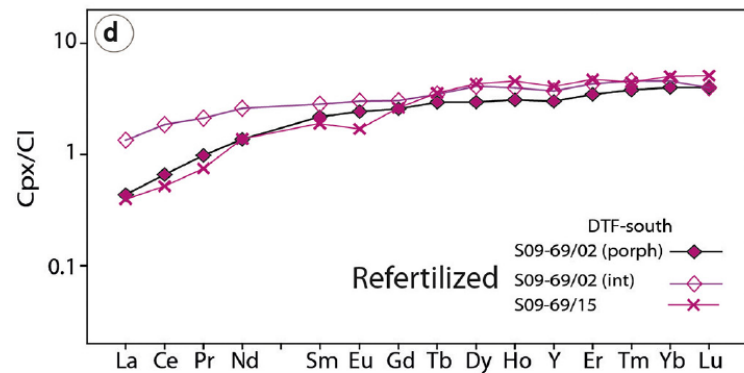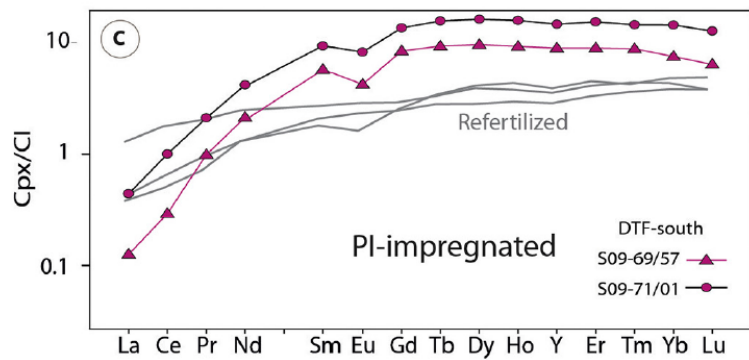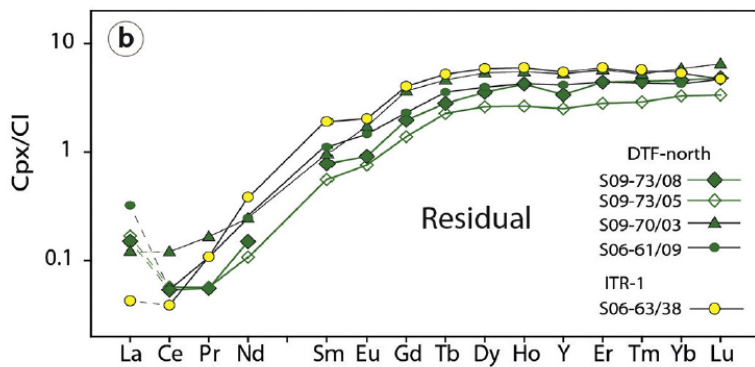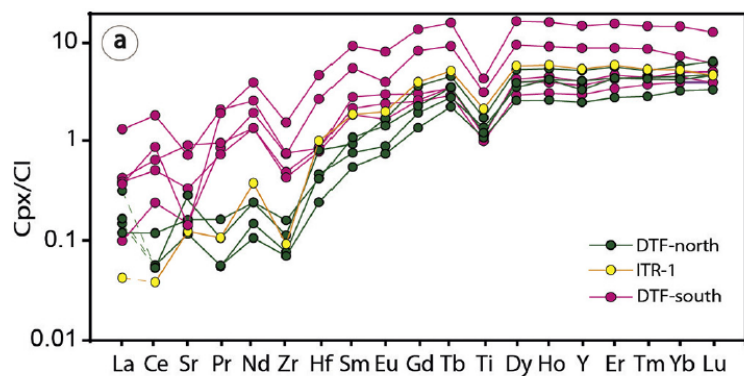
954   Fig. 2

955
956

957   Fig. 3

958
959

960   Fig. 4

961
962

963   Fig. 5

964
965
966
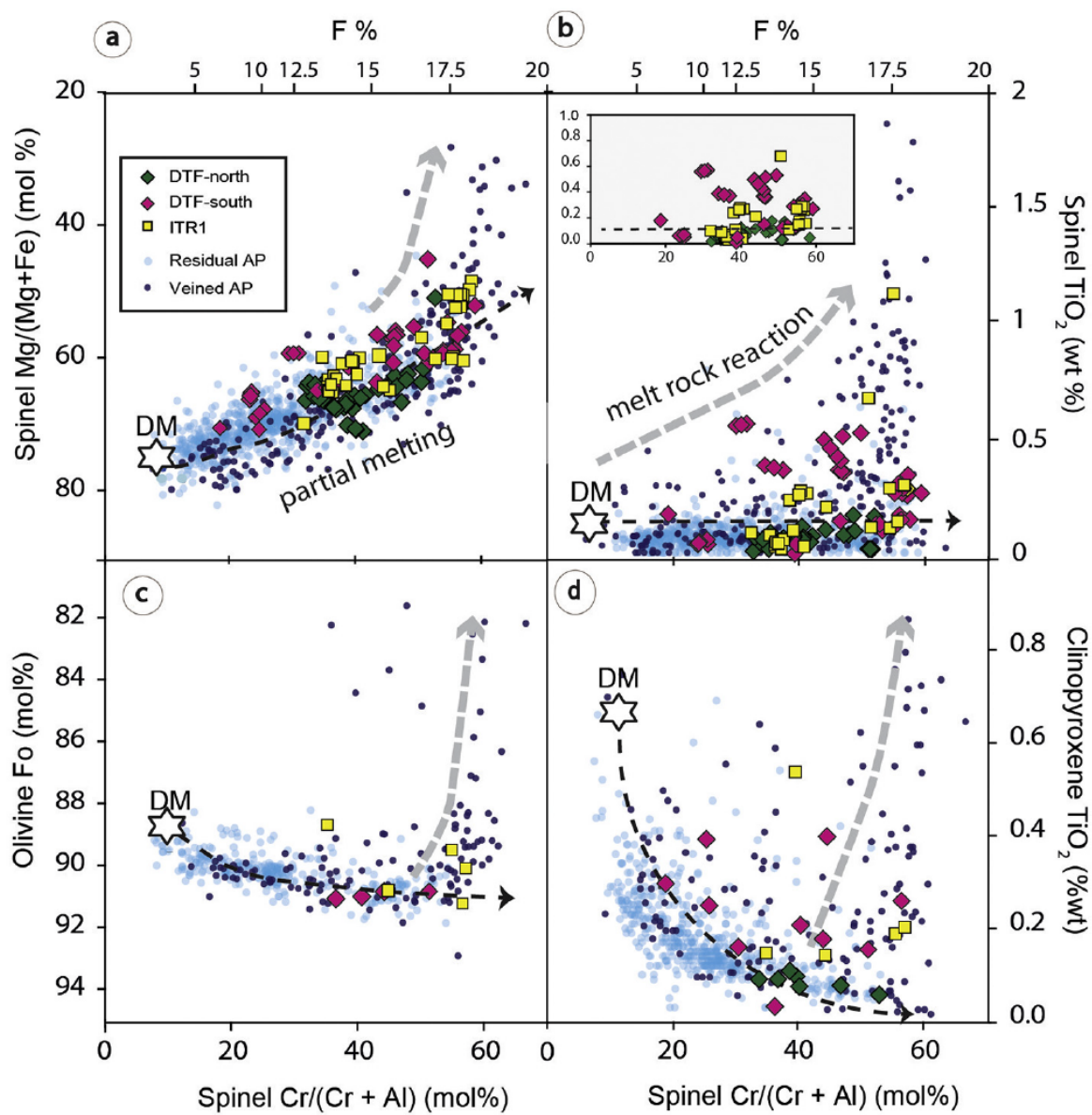
967   Fig. 6

968
969

970   Fig. 7

971

972   Fig. 8

a Plate model - N-MORB (Gale et al., 2013)

b Plate model - Single melt increment (8%)

c Plate model - Ultra-depleted Melt
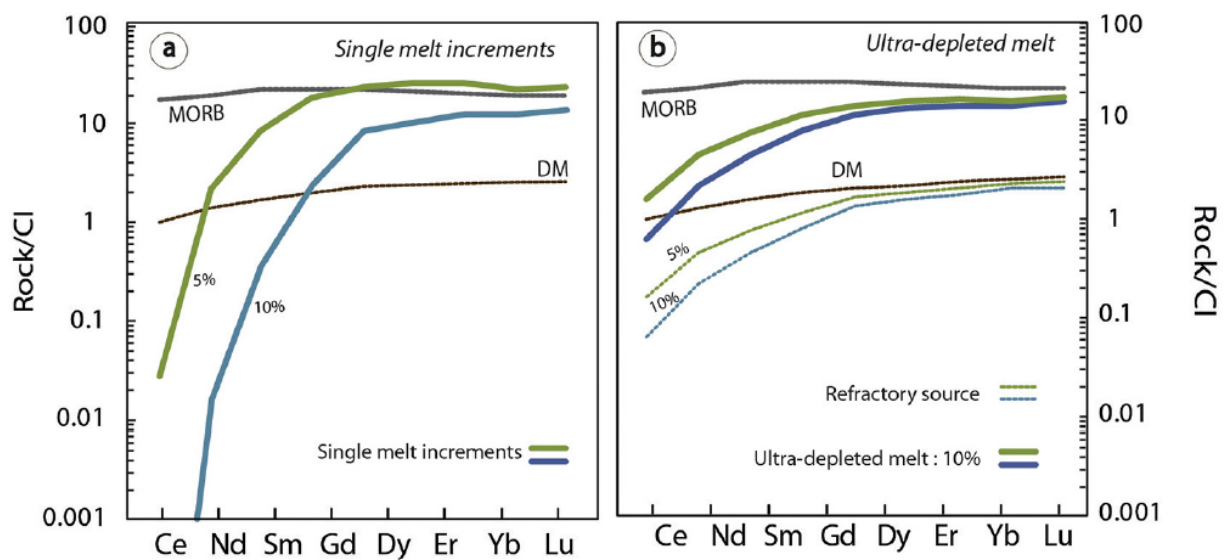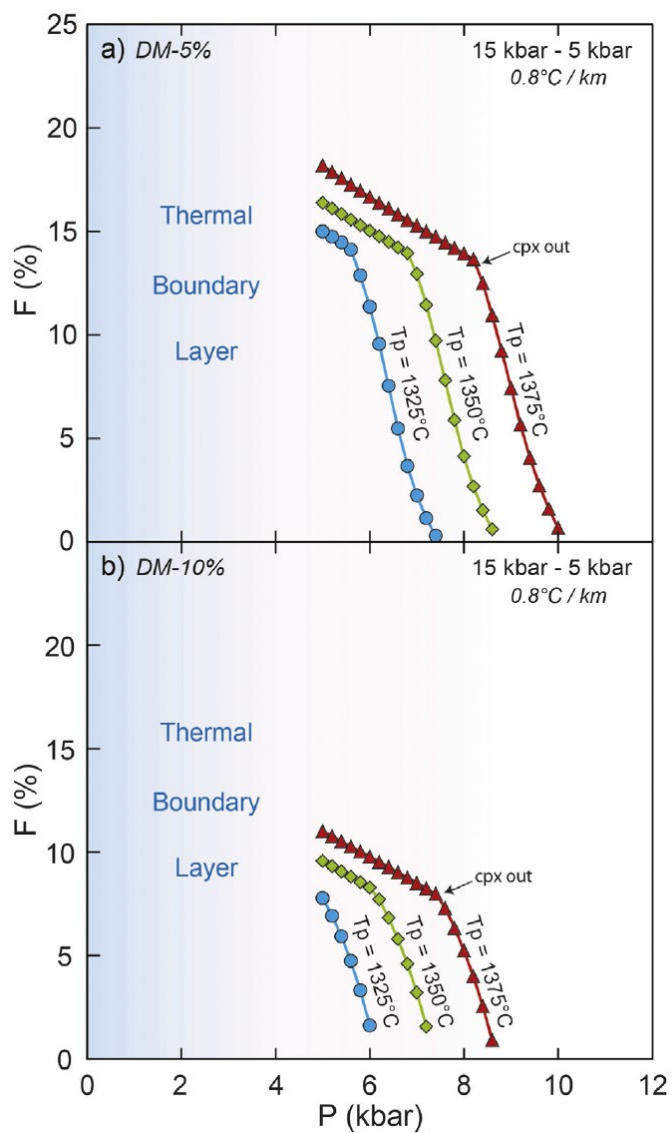
d Plate Model - closure of the system
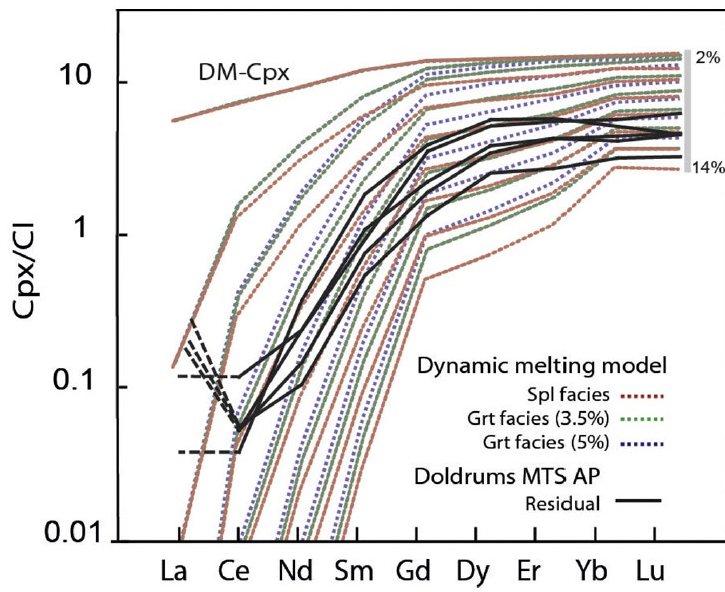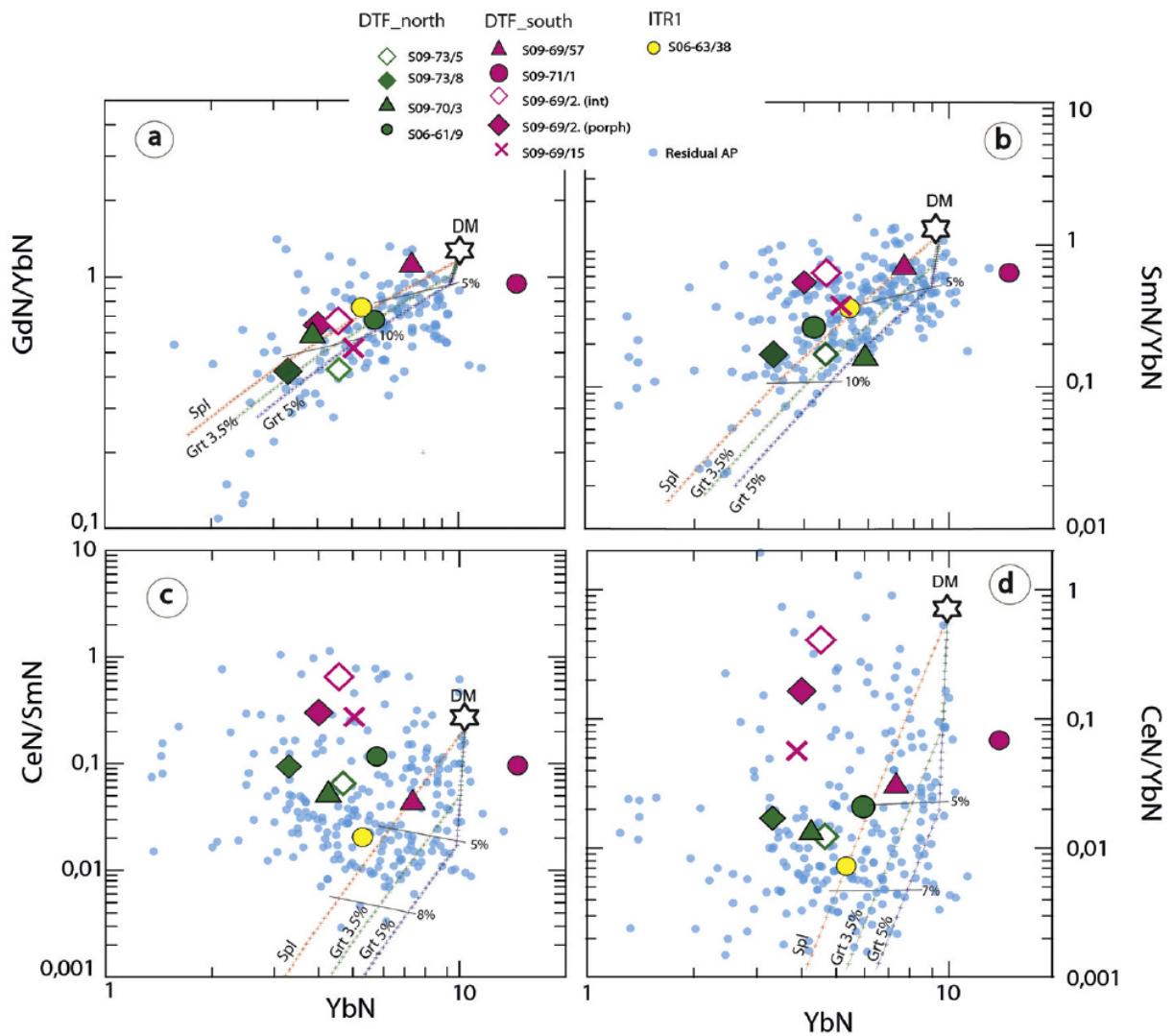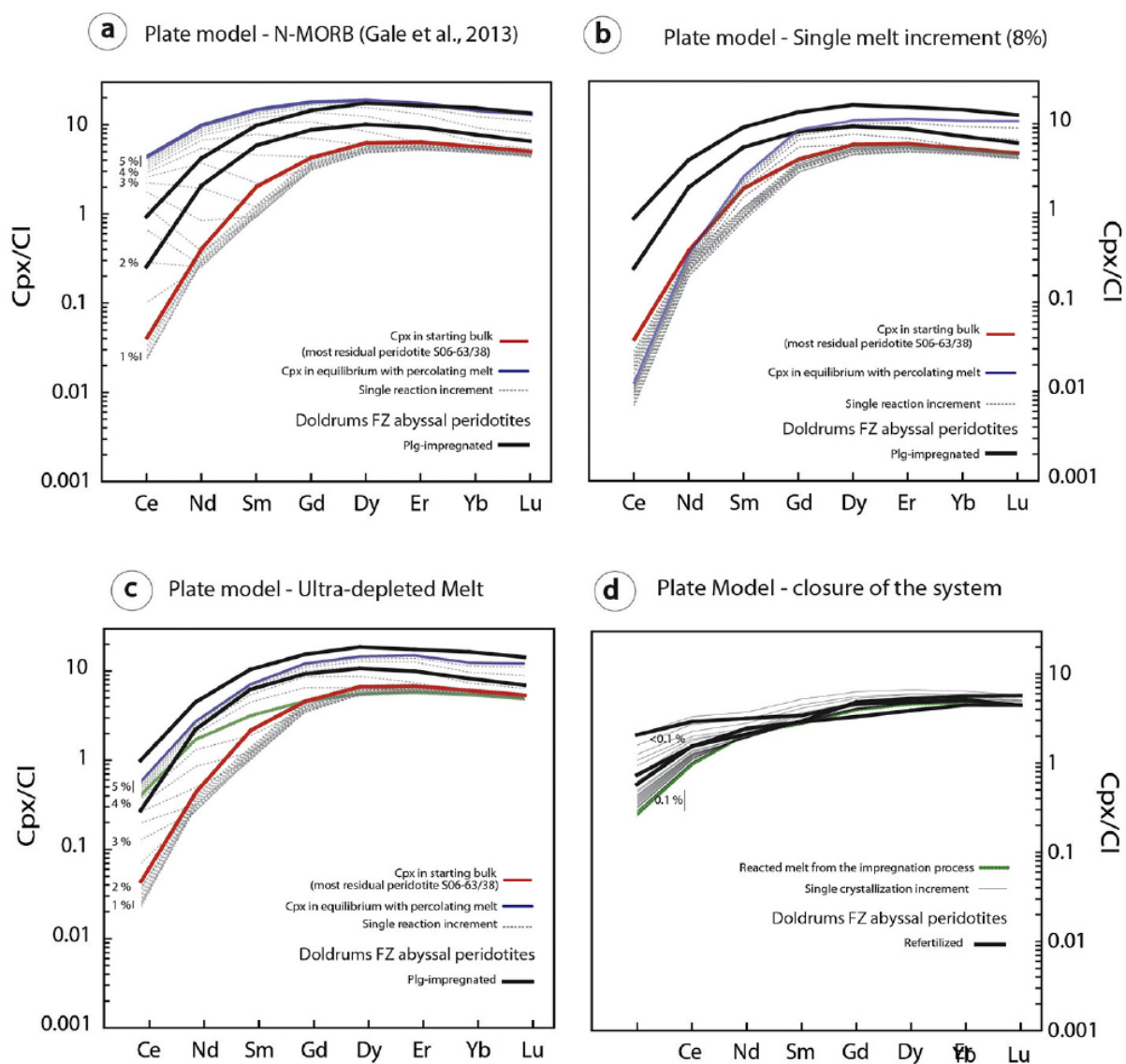
973
974
975

976   Fig. 9

977
978
979   Fig. 10

980